Identification of Cellular Protein Targets of a Half-Sandwich Iridium(III) Complex Reveals Its Dual Mechanism of Action via Both Electrophilic and Oxidative Stresses

Robin Ramos, Anthi Karaiskou, Candice Botuha, Sadek Amhaz, Michaël Trichet, Florent Dingli, Jérémy Forté, France Lam, Alexis Canette, Chloé Chaumeton, et al.

Identification of Cellular Protein Targets of a Half-Sandwich Iridium(III) Complex Reveals its Dual Mechanism of Action via Both Electrophilic and Oxidative Stresses

Robin Ramos,[1] Anthi Karaiskou,[1] Candice Botuha,[2] Sadek Amhaz,[1] Michaël Trichet,[3] Florent Dingli,[4] Jérémy Forté,[2] France Lam,[3] Alexis Canette,[3] Chloé Chaumeton,[3] Murielle Salome,[5] Thomas Chenuel,[6] Céline Bergonzi,[6] Philippe Meyer,[6] Sylvain Bohic,[7] Damarys Loew,[4] Michèle Salmain,[2,†] and Joëlle Sobczak-Thépot[1, *]

[1]Sorbonne Université, INSERM, Centre de Recherche Saint Antoine, 184 rue du Faubourg Saint Antoine, F-75012 Paris, France.
[2]Sorbonne Université, CNRS, Institut Parisien de Chimie Moléculaire, 4 place Jussieu, F-75005 Paris, France.
[3]Sorbonne Université, CNRS, Institut de Biologie Paris-Seine, Service d'imagerie cellulaire, F-75005, Paris.
[4]Institut Curie, PSL Research University, CurieCoreTech Mass Spectrometry Proteomics, F-75248 Paris, France.
[5]ESRF, The European Synchrotron Research Facility, F-38043 Grenoble cedex 9, France.
[6]Sorbonne Université, PSL, CNRS, UMR8226, Institut de Biologie Physico-Chimique, Laboratoire de Biologie Moléculaire et Cellulaire des Eucaryotes, F-75005 Paris, France.
[7]Université Grenoble Alpes, INSERM, UA7 STROBE, Synchrotron Radiation for Biomedicine, F-38400 Saint Martin d'Hères, France.

[†] Correspondence: michele.salmain@sorbonne-universite.fr
[*] Correspondence: joelle.sobczak@inserm.fr

Abstract

Identification of intracellular targets of anticancer drug candidates provides key information on their mechanism of action. Exploiting the ability of the anticancer (C^N)-chelated half-sandwich iridium(III) complexes to covalently bind proteins, click chemistry with a bioorthogonal azido probe was used to localize a phenyloxazoline-chelated iridium complex within cells and profile its interactome at the proteome-wide scale. Proteins involved in protein folding and actin cytoskeleton regulation were identified as high affinity targets. Upon iridium complex treatment, the folding activity of Heat Shock Protein HSP90 was inhibited *in vitro* and major cytoskeleton disorganization was observed. A wide array of imaging and biochemical methods validated selected targets and provided a multiscale overview of the effects of this complex on live human cells. We demonstrate that it behaves as a dual agent, inducing both electrophilic and oxidative stresses in cells that account for its cytotoxicity. The proposed methodological workflow can open innovative avenues in metallodrug discovery.

Keywords: chemical proteomics, bioorthogonal chemistry, click chemistry, X-ray fluorescence, correlative electron microscopy, cell adhesion, chaperone, oxidative stress

Introduction

Uncovering metal-based alternatives to platinum anticancer drugs is an active research area as oncologists are still in need of molecules with an original mode of action and less side effects. Iridium(III) complexes are actively investigated to this purpose[1] with two main families of molecules under current study, namely the kinetically inert photoluminescent bis-cyclometalated complexes[2–4] and the so-called half-sandwich complexes comprising a penta-substituted cyclopentadienyl ligand. The coordination sphere of this latter class of compounds is generally completed by a bidentate chelating ligand and an exchangeable halogeno ligand.[5–10]

Importantly, the lability of the halogeno ligand of some half-sandwich iridium complexes provides them with a reactivity towards various cellular substrates. The first recognized cellular substrate was NADH, whose catalytic oxidation is responsible for the production of H_2O_2 from O_2 by hydride transfer[11] demonstrated both *in vitro* and *in vivo*[12,13]. While other potential cellular targets were investigated, such as the tripeptide GSH (via its central cysteine residue),[14] calmodulin (via some of its methionines)[15] and the redox enzyme thioredoxin reductase,[16] no general approach has been undertaken to allow the unbiased identification of the targets of half-sandwich iridium complexes *in vivo*.

We previously introduced a series of 10 half-sandwich complexes including diversely substituted phenyloxazoline (phox) chelating ligands. From the subsequent structure-activity relationship (SAR) study, **Ir2** carrying a dimethyl substituent on the oxazoline ring was identified as the best hit amongst the series in terms of overall cytotoxicity, inhibition of proliferation, apoptosis induction and H_2O_2 production, both *in vitro* and *in vivo.*[13]

We also designed a half-sandwich iridium complex comprising a modified phenyloxazoline ligand to which was appended a BODIPY entity, so as to address the drug to membrane-rich organelles.[17] Thanks to its fluorescent properties, the complex was localized in the endoplasmic reticulum and mitochondrial membranes. Most importantly, we could demonstrate that this complex

forms covalent adducts with a subset of intracellular proteins via a ligand exchange mechanism. The ability of phenyloxazoline-chelated half-sandwich iridium complexes to both bind covalently to proteins and to generate oxidative stress prompted us to develop new strategies to elucidate their mechanism of action, to identify their intracellular protein targets and investigate their relevance in terms of protein function and cellular behavior.

In recent years, metalloproteomics has emerged as a powerful tool to identify the cellular protein targets of various anticancer metal-based drugs.[18–20] Different workflows have been designed, the most advanced ones relying on bioorthogonal probes, combined with protein pull-down, shotgun LC-MS/MS analysis and database interrogation for protein identification. The first step of this workflow can be performed either with cell lysates[21–25] or with live cells[26]. This latter strategy has been applied to uncover the main protein targets of inert gold(III)[27,28] and bis-cyclometalated iridium(III)[29] complexes using photoaffinity probes, but also of arsenic trioxide[30,31] in cancer cells and cisplatin in yeast[32] using azido derivatives.

Herein we report the identification of **Ir2** main protein targets using an insightful and unbiased chemoproteomics approach. Two half-sandwich iridium bioorthogonal probes **IrN$_3$** and **Ir2N$_3$** were synthesized (**Figure 1A**), comprising a minimally invasive azido function, ready to undergo chemoselective ("click") ligations with relevant partners. For this, the well-known copper-catalyzed [3+2] azide-alkyne cycloaddition (CuAAC) on the iridium probes was performed for fluorescence imaging and for partner protein enrichment followed by identification using quantitative mass spectrometry (**Figure 1B**). In combination with an array of approaches including multiscale cell imaging and *in vitro* assays, this study uncovers the main cellular processes that are altered by this class of complexes, providing molecular bases for their cytotoxicity.

Results

The dimethyl substituents on the chelating ligands of Ir2 and Ir2N$_3$ are essential for their *in vitro* reactivity

The two bioorthogonal probes **IrN$_3$** and **Ir2N$_3$** (**Figure 1A**) were synthesized in two or three steps from 2-(4-(chloromethyl)phenyl)-4,5-dihydrooxazole or 2-amino-2-methyl-1-propanol, respectively. Both **IrN$_3$** and **Ir2N$_3$** crystallized in the monoclinic $P2_{1/n}$ space group (**Table S1**). Their molecular structure shows the classical piano-stool geometry around the iridium atom (**Figure S1A**). ^{1}H NMR monitoring of solutions of **Ir2**, **IrN$_3$** and **Ir2N$_3$** in DMSO-d_6 showed that they all rapidly evolved to the cationic DMSO complexes by chlorido to DMSO ligand exchange with half-lives of 5, 10 and 11 min, respectively (**Figure S1B, Figure S2**). The DMSO complex **Ir2-DMSO** derived from **Ir2** was independently obtained by chloride abstraction with $AgNO_3$, followed by addition of DMSO. Its molecular structure shows that DMSO coordination occurs by its S rather than by its O atom (**Figure S1A**). Formation of solvento adducts of **Ir2** was also qualitatively observed by uv-visible spectroscopy upon dilution of a methanolic solution of **Ir2** in water or DMSO (**Figure S3A**).

Formation of covalent adducts by reaction of **Ir2** with various amino-acids and side chain models in MeOH/water mixture was probed *in vitro* by ESI-HRMS in positive ionization mode. Expectedly, **Ir2** did not form adducts with alanine and proline, however they were systematically observed for amino-acids comprising a sulfur or nitrogen donor atom on their side chain (N-acetyl histidine, **Figure S1C** and N-acetyl cysteine methyl ester, **Figure S1D**). In addition, formation of an adduct between **Ir2** and L-methionine, by coordination of its sulfur atom, was evidenced by ^{1}H NMR spectroscopy (**Figure S1E**). Formation of monovalent adducts is a direct consequence of the easy exchange of the chlorido ligand in **Ir2**, in sharp contrast with bis-cyclometalated complexes that are kinetically inert.

Reactivity of **Ir2-DMSO** (formed by dissolution of **Ir2** in DMSO) was examined by RP-HPLC. We found that **Ir2-DMSO** was stable in H_2O and DMEM containing 0.5% DMSO (i.e. 7 mM) after 30 min at 37°C (**Figure S3B-C**). RP-HPLC analysis of mixtures of **Ir2-DMSO** and 10 mole equiv. N-acetyl cysteine methyl ester, N-acetyl methionine methyl ester, N-acetyl histidine or a mixture of the three amino acid derivatives in water containing 0.5% DMSO showed the formation of a single adduct with N-acetyl cysteine methyl ester via DMSO ligand exchange (**Figure S3D-H**). The apparently divergent reactivity of **Ir2** and **Ir2-DMSO** towards amino acids reflects the respective ability of the Cl/H_2O and DMSO ligands to be exchanged by other donor ligands. Since DNA is a known target of metal-based drugs like cisplatin, interaction of **Ir2** with DNA was investigated by circular dichroism (CD) spectroscopy. Solutions of ct-DNA were incubated with 1 mole equiv. **Ir2** (with respect to nucleotide content), cisplatin (as a model of DNA covalent binder) or DAPI (as a model of DNA intercalator) for 24 h at 37°C and the near-uv CD spectrum of each solution was recorded (**Figure S3I**). Unlike cisplatin and DAPI, **Ir2** did not induce any change of the CD spectrum of ct-DNA, indicating that no interaction takes place between this complex and DNA.

Interestingly, our previous SAR study showed that **Ir2** was able to spontaneously produce H_2O_2 in the cell cytoplasm via a catalytic mechanism presumably combined to depletion of intracellular NAD(P)H. Herein, we checked whether its congeners **IrN$_3$** and **Ir2N$_3$** displayed the same feature *in vitro* (**Figure S1F**). Confirming our previous observations, we found that **Ir2** and **Ir2N$_3$** were more potent than **IrN$_3$** to catalytically produce H_2O_2 from NADH and O_2 in model conditions, highlighting again the importance of the dimethyl substituent on the oxazoline ring for pro-oxidant activity.

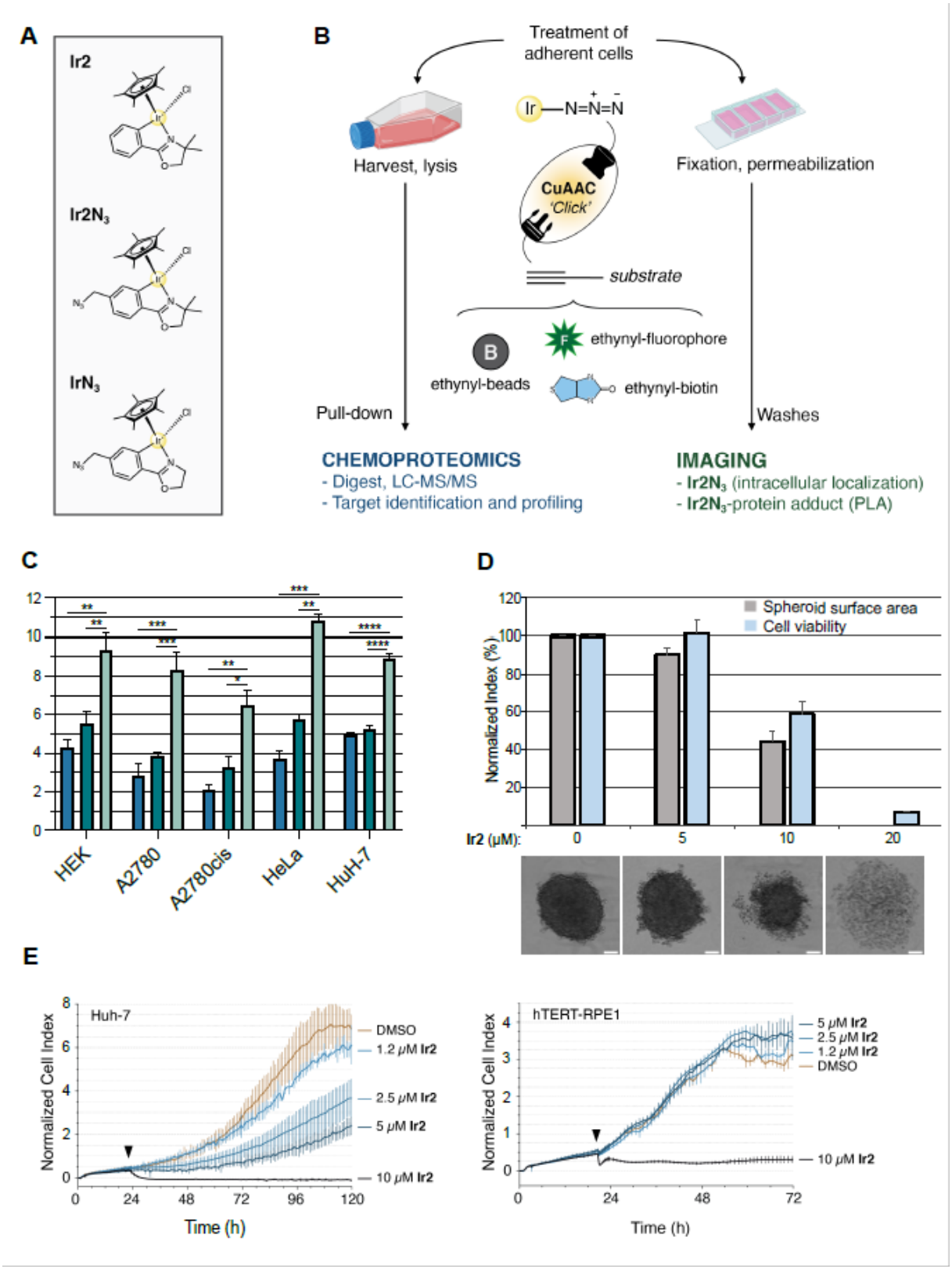

Figure 1. Experimental design and anti-proliferative activity of iridium compounds

(**A**) Half-sandwich complexes used in this study (**Ir2**, **IrN_3**, **$Ir2N_3$**).

(**B**) Experimental strategy using CuAAC ($CuSO_4$, THPTA, sodium ascorbate) with ethynyl-substituted substrates to perform chemoproteomics and cell imaging (created with BioRender.com).

(**C**) Histograms representing the IC_{50} of the three complexes in various cell lines given in μM as mean ± SEM of at least three replicates (seeding 4,000 cells/well, endpoint 72 h, alamarBlue assay).

(**D**) Images of HeLa cell spheroids treated with increasing concentrations of **Ir2** for 6 days are shown alongside histograms displaying spheroid surface area and viability assessed by alamarBlue assay, both expressed as percentages of the values in the untreated control. Scale bar = 100 μm

(E) Real time cell analysis (RTCA) curves of Huh-7 and hTERT-RPE1 cells treated with the indicated concentrations of **Ir2** or vehicle (DMSO).

Ir2, $Ir2N_3$ and IrN_3 exhibit contrasting anti-proliferative and pro-oxidant properties

We previously showed that **Ir2** inhibited HeLa cell proliferation and induced a rapid activation of caspases, resulting in apoptotic cell death with an IC_{50} value around 4 µM.[13] Accordingly, around 50 % of HeLa cells exposed to 4 µM **Ir2** for 72 h were viable with an intact plasma membrane **(Figure S4**). **Ir2** cytotoxicity was also assayed in HeLa cells using a classical 2D clonogenicity assay (**Figure S5**). **Ir2** dramatically reduced the ability of cells to form colonies even at a concentration of 1.25 µM, *i.e.* below the IC_{50}. In addition, only 20 % of the cells were still able to survive and form colonies after a transient 24 h exposure to 4 µM **Ir2**, consistent with the results of the above survival assays. Finally, we examined the effect of **Ir2** on HeLa cell spheroids, a model that better resembles *in vivo* tumor conditions. As anticipated, spheroids exhibited greater resistance to **Ir2** in 3D compared to 2D cultures, with an IC_{50} value being 2.5 times higher in spheroids (~10 µM) than in 2D monolayers (4 µM) (**Figure 1D**).

To determine the efficiency of **Ir2** accumulation in HeLa cells, elemental iridium concentration was assayed by Inductively Coupled Plasma - Optical Emission Spectrometry (ICP-OES). The intracellular content of iridium was found to be dose-dependent with 405 ± 3 and 855 ± 14 ng of **Ir** per 10^6 cells after 30 min of exposure to 5 and 10 µM, respectively, indicating an efficient intracellular accumulation of the compound. Co-incubation with the metabolic inhibitors CCCP (Carbonyl cyanide m-chlorophenyl hydrazone), 2-DG (2-deoxyglucose), or both, did not significantly modify the intracellular concentration of iridium (**Table S2**), demonstrating that cell uptake occurred by passive diffusion through the plasma membrane. Consistently, the lipophilic character of **Ir2** and its congeners **$Ir2N_3$** and **IrN_3** was substantiated after measurement of the octanol-water partition coefficient (log *P*) of their DMSO adducts, respectively equal to 5.2, 5.4 and 3.7, as measured by the OECD HPLC method.[33]

We then compared the effects of **Ir2**, **Ir2N$_3$** and **IrN$_3$** on a selected panel of human cell lines. As in our previous studies, the HeLa (late-stage cervix adenocarcinoma) and near-diploid hTERT-RPE1 (telomerase-immortalized retinal pigment epithelial cells) cell lines were used as models of tumoral and non-tumoral cells, respectively. The panel was completed with the hepatocarcinoma Huh-7 and the ovarian carcinoma A2780 and its cisplatin resistant derivative A2780cis, representative of a highly sensitive cell line.[34] The HEK293 cell line (adenovirus-immortalized human embryonic kidney cells) that displays a broad spectrum of expressed proteins was chosen for chemoproteomics.

The median inhibitory concentration (IC_{50}) of cell proliferation was evaluated for each complex (**Figure 1C, Table S3**), showing ranges of IC_{50} comprised between 2 and 6 μM for **Ir2** and **Ir2N$_3$** and between 6 and 11 μM for the less cytotoxic **IrN$_3$**. Interestingly, the iridium-based drugs were potent in both cisplatin-resistant and sensitive A2780 cells. Furthermore, in all cell lines, **Ir2** and **Ir2N$_3$** displayed similar IC_{50} values, confirming that **Ir2N$_3$** is an appropriate surrogate to probe the intracellular effects of **Ir2**. Real Time Cell Analysis (RTCA) of live cell adhesion and proliferation in a label-free assay showed that **Ir2** inhibited cell proliferation in a dose-dependent manner (Huh-7 cell line, **Figure 1E**). Of note, at high concentration (10 μM), **Ir2** triggered a very rapid loss of cell adhesion and hence viability. In contrast, nontumoral hTERT-RPE1 cells displayed a distinct, all-or-nothing response to **Ir2**, as cells survived and proliferated when exposed to 5 μM **Ir2** but rapidly lost adhesion (**Figure 1E**) and died within 180 min (**Figure 2D**) when exposed to 10 μM **Ir2**.

The fluorescent H_2O_2-selective ratiometric probe "HyPer" developed by Belousov et al.[35] was used to confirm the pro-oxidant properties of **Ir2** and **Ir2N$_3$** *in cellulo* (**Figure 2A**). The fluorescence properties of HyPer change upon its reversible oxidation by H_2O_2 and reduction by glutathione-dependent reductases, thus monitoring intracellular hydrogen peroxide levels expressed as HyPer index.[13] Cells exposed to 100 μM H_2O_2 as positive control exhibited a fast recovery as the HyPer index returned to its basal value within one hour. In contrast, upon treatment with **Ir2** and **Ir2N$_3$** in the same time lapse, the HyPer index rose progressively, indicating a continuous catalytic production of H_2O_2

and/or defective detoxification processes by the cells challenged with the drugs. **IrN$_3$** was less active in this assay, consistent with its higher IC_{50}. These results are in full agreement with the respective ability of the complexes to oxidize NADH *in vitro* (**Figure S1F**).

ROS production in cells is known to elicit the antioxidant response, marked by the accumulation and activation of Nuclear factor erythroid 2-Related Factor (Nrf2).[36] Western blot analysis (**Figure 2B**) showed that, in the HEK293 cell line, only **Ir2** and **Ir2N$_3$** were able to induce a mild upregulation of the transcription factor that was sustained throughout 24 h of treatment. In hTERT-RPE1 cells (**Figure 2C**), a higher increase of Nrf2 was observed in response to **Ir2** with respect to the azido-substituted complexes, consistent with the respective IC_{50} of the three complexes. Moreover, hTERT-RPE1 cells were markedly able to cope with electrophilic or oxidative stress induced by the complexes, with Nrf2 returning to basal levels after 24 h.

The lipophilic and cationic nature of the **Ir2**-DMSO complex led us to predict a mitochondrial tropism. Mitochondrial membrane potential progressively decreased within 180 min in hTERT-RPE1 cells in the presence of 10 μM **Ir2**, in parallel with cell death (**Figure 2D-E**). The morphology of mitochondria was analyzed using an antibody targeting TOMM20 (Translocase of Outer Mitochondrial Membrane 20) (**Figure 2F**). Untreated control cells displayed the typical distribution of mitochondria, forming filamentous structures throughout the cytoplasm. However, after 24 h of treatment with 4 μM of **Ir2**, a dose that is below the toxic threshold of 10 μM, mitochondria showed a more condensed and round pattern, indicative of mitochondrial stress, that could also contribute to ROS production.[37]

Once generated, ROS can diffuse throughout the cell and indirectly induce DNA double strand breaks.[38] Therefore, we monitored the presence of phosphorylated histone H2AX (γ-H2AX) foci marking regions of DNA double strand breaks in HeLa and hTERT-RPE1 cells treated with **Ir2**. Conversely to Etoposide, used as positive control, **Ir2** did not significantly increase the number of

DNA damage foci within 48 h (**Figure S6**), suggesting that the DNA damage response pathway is not directly implicated in cytotoxicity.

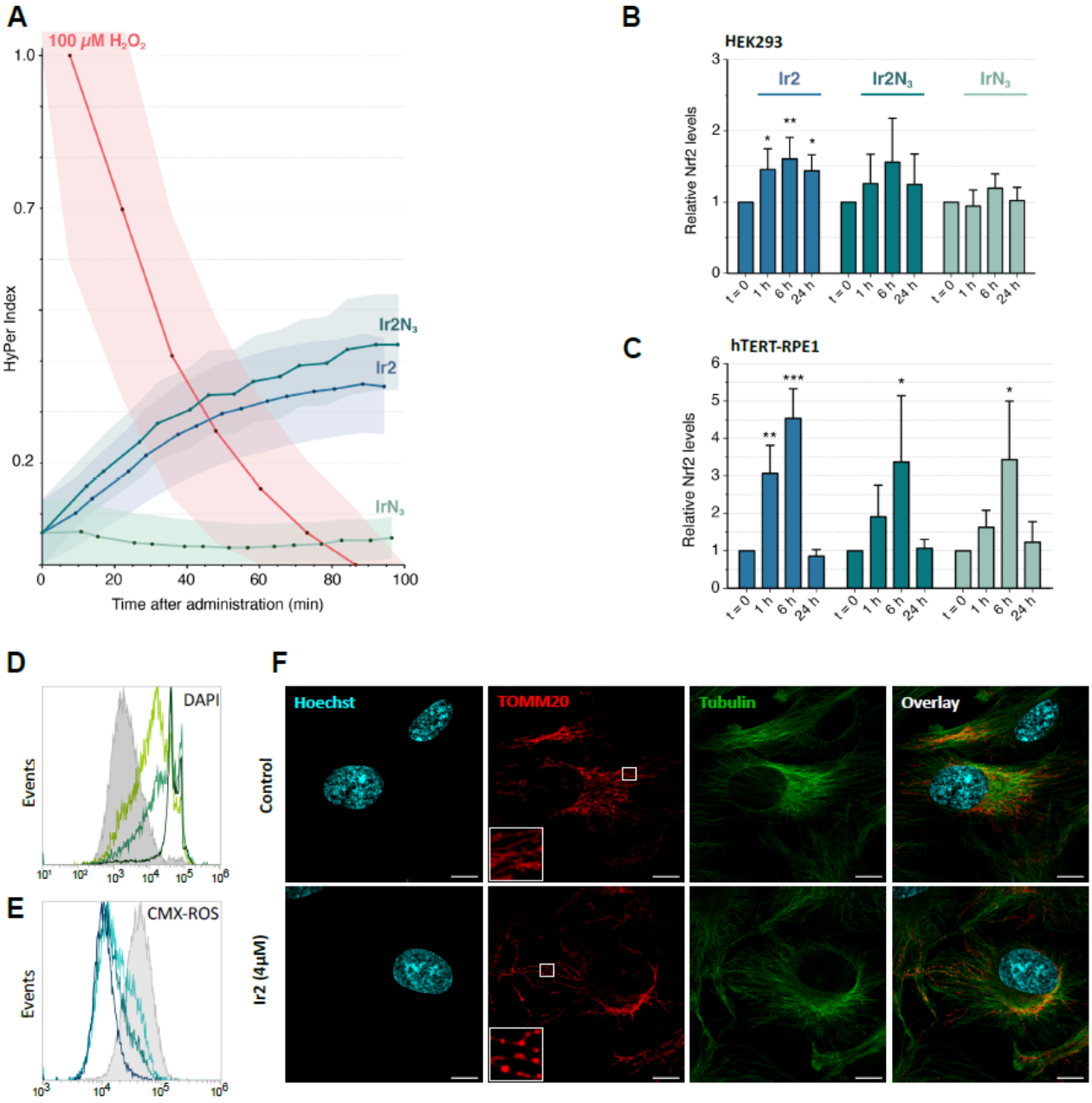

Figure 2. Iridium compounds elicit contrasting production of H_2O_2 and antioxidant response

(**A**) Real-time monitoring of the HyPer index in live cells treated with H_2O_2, **Ir2**, **Ir2N$_3$,** or **IrN$_3$**. A stable HeLa cell line that constitutively expresses the H_2O_2 probe HyPer was exposed to the three complexes, then reduced and oxidized forms of HyPer were quantified by flow cytometry as the ratio of fluorescence emission at 520 nm after excitation at 405 and 488 nm respectively. The mean ratios of the HyPer-expressing cells (N = 5,000 – 10,000) were used to calculate a HyPer index relative to the negative (DMSO) and positive (H_2O_2) controls.

Western Blot analysis of the antioxidant response in (**B**) HEK293 and (**C**) hTERT-RPE1 cells. Semi-quantification of Nrf2 levels following exposure to the three complexes during 1, 6 or 24 h, relative to untreated cells (t = 0) and calculated from at least 3 independent experiments. Statistical significance was calculated using one-way analysis of variance with a Dunnett's post-test compared to t=0 (*p < 0.05; **p < 0.01; ***p < 0.001).

Histograms showing flow cytometry analyses of hTERT-RPE1 cells treated with 10 µM **Ir2** for 45, 90 and 180 min compared to control untreated cells (grey). (**D**) DAPI dye exclusion assay showing the time dependent accumulation of DAPI-positive dead cells; light green, 45 min; medium green, 90 min; dark green 180 min. The percentage of viable cells decreased from 97% in untreated cells to 62, 40 and 11% respectively. (**E**) Mitotracker Red CMX-ROS staining showing the time dependent decrease of mitochondrial labeling indicating a decrease of membrane potential; light blue, 45 min; medium blue, 90 min; dark blue 180 min. The percentage of cells with active mitochondria (fluorescence above 2.10^4) decreased from 93% in untreated cells to 41, 27 and 9% respectively.

(**F**) Confocal images of hTERT-RPE1 cells treated or not with 4µM of **Ir2** during 24 hours. Labeling of mitochondria with Translocase of Outer Mitochondrial Membrane 20 (TOMM20, red), microtubules (α-Tubulin, green) and nucleus (DNA, Hoechst 33342, cyan). Zoom on a selected region showing morphological alterations of mitochondria in **Ir2** treated cells. Scale bar = 10µm

Click-based chemoproteomics generates a comprehensive list of direct protein targets of $Ir2N_3$

HEK293 cells were cultivated for 20 min in the presence of **$Ir2N_3$** at 0.2 and 5.0 µM, to assess for dose-dependent effects, and compared to untreated cells. A click-on-resin strategy was employed to pull down proteins covalently bound to **$Ir2N_3$** by copper-catalyzed azide-alkyne cycloaddition (CuAAC) with ethynyl-substituted agarose beads. After on-bead trypsin digestion, mass spectrometry analysis of the samples, each in quintuplicate, led to the absolute quantification of 3686 proteins at the concentration of 5 µM **$Ir2N_3$**, 2140 proteins at 200 nM **$Ir2N_3$**, and 1594 proteins in the control sample, expressed in molar percentage (Absolute quantification, **Figure S7A**). In the differential analysis, proteins enriched in the iridium-treated samples were selected according to the criteria of at least 2 distinct peptides in 3 replicates with a fold change ≥ 1.5 compared to the control and a p-value ≤ 0.05. 211 proteins were selected from the 200 nM treated sample and termed high affinity targets (List A, **Table S4**) while proteins selected from the 5 µM treated sample constituted List B. As expected, 96% of the proteins from List A were also present in List B. Proteins belonging to List B but not List A were compared according to their fold change between 0.2 and 5.0 µM conditions. In this comparison, 388 proteins having a fold change comprised between 1 and 16 were qualified as intermediate affinity targets, and 786 proteins only captured at 5 µM were defined as low affinity targets (**Figure S7B**).

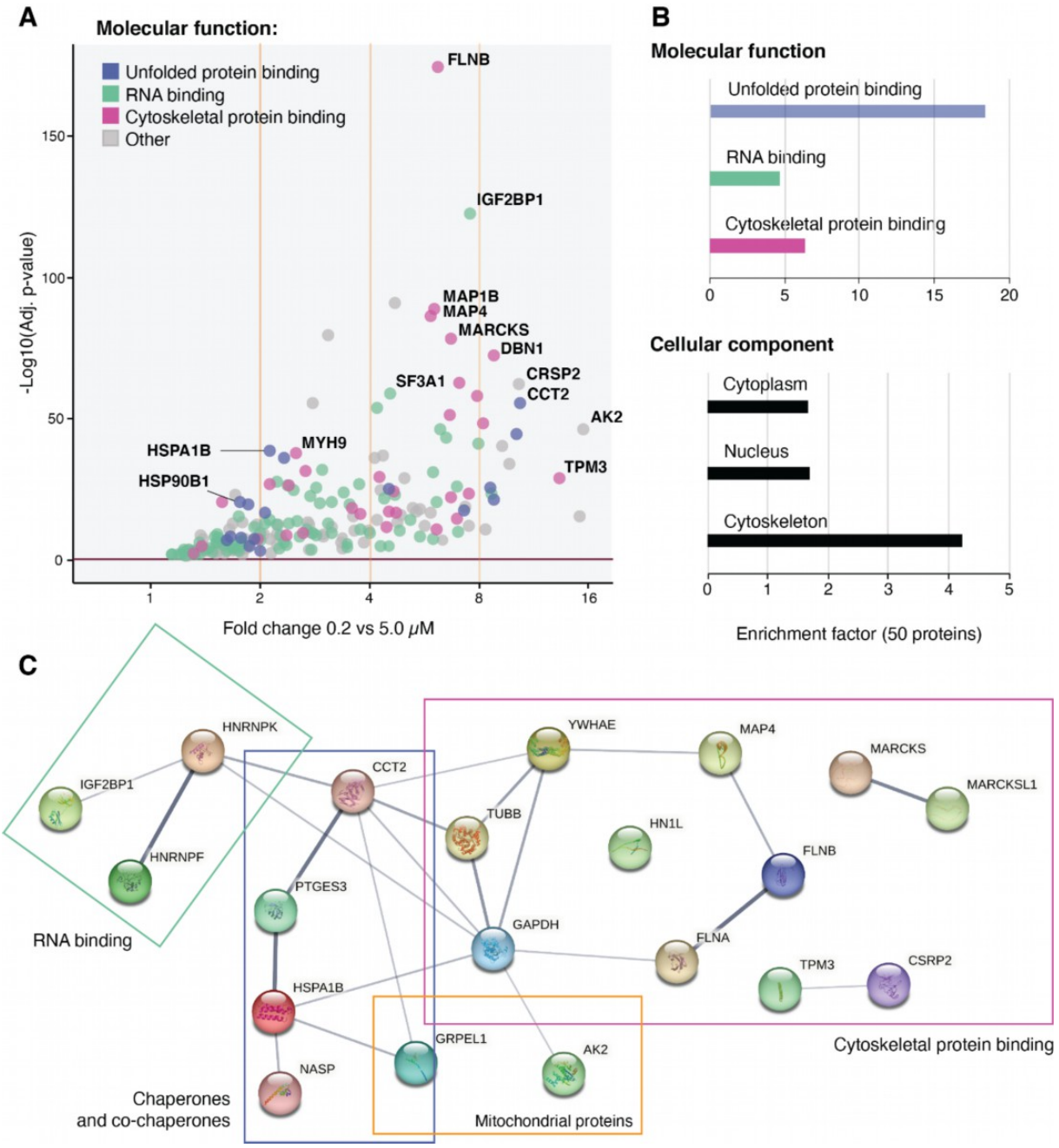

Figure 3. Click-based chemoproteomics generates a comprehensive list of direct protein targets of Ir2N$_3$

(**A**) Volcano plot showing statistical significance (*p* value) versus magnitude of change (fold change) for the 211 "high affinity" targets captured at two concentrations of **Ir2N$_3$** in HEK293 cells. Color-annotation of the most represented molecular functions.

(**B**) Ratio between the set and background frequency of representative GO annotations in each category, performed over the 50 most abundant proteins amongst the high affinity targets, according to their absolute quantification in the 5 µM condition.

(**C**) STRING map of the interaction network between the 20 most abundant proteins amongst the high affinity targets, according to their absolute quantification in the 5 µM condition.

High-affinity targets ranked according to their fold change between 0.2 and 5.0 µM conditions and p-value are shown in the volcano plot, **Figure 3A**. GO term analysis was used to highlight the predominant molecular functions amongst these 211 targets. Cytoskeletal protein binding (GO:0008092), RNA binding (GO:0003723) and Unfolded protein binding (GO:0051082) were the most significant categories (p value $\leq 6.10^{-6}$). The 50 most abundant high affinity targets were selected according to their absolute quantification in the 5.0 µM condition for further GO analyses. Proteins with GO terms "Unfolded protein binding" and "Cytoskeleton" in the respective categories molecular function and cellular component, displayed the highest enrichment compared to their background frequency in the human proteome (**Figure 3B**). According to the Cellular Component GO analysis, these 50 targets were found in the cytoplasm and in a variety of organelles (nucleus, mitochondria, ER).

The 20 most abundant high affinity targets are shown in the STRING interaction map (**Figure 3C**). Interestingly, the same GO terms are represented within this reduced list, containing 5 chaperones and co-chaperones, 3 RNA-binding proteins and 11 proteins related to cytoskeleton, including mostly actin binding proteins. In addition, two mitochondrial proteins are present, AK2 and GRPEL1.

X-ray fluorescence microscopy reveals a pan-cellular distribution of Ir2

To obtain an unbiased view of the sites of accumulation of **Ir2** in hTERT-RPE1 living cells, we used an advanced method of cryo-fixation followed by synchrotron high resolution X-ray fluorescence (XRF) mapping of elements at the ID16a beamline of ESRF (**Figure 4A and Figure S8A**). This method preserves all intracellular elements including the highly diffusible ions like K (uniform subcellular distribution[39]) and highlights several compartments such as the nucleus with P and Zn and the Golgi apparatus with Mn (stored at physiological level in the Golgi apparatus in human cells[40,41]). The mapped XRF signal of iridium was readily detected in the cytoplasm and the nucleus and appeared enriched on structures identified as mitochondria, actin bundles and nuclear envelope when compared to cryo-optical fluorescence microscopy using vital markers.[42]

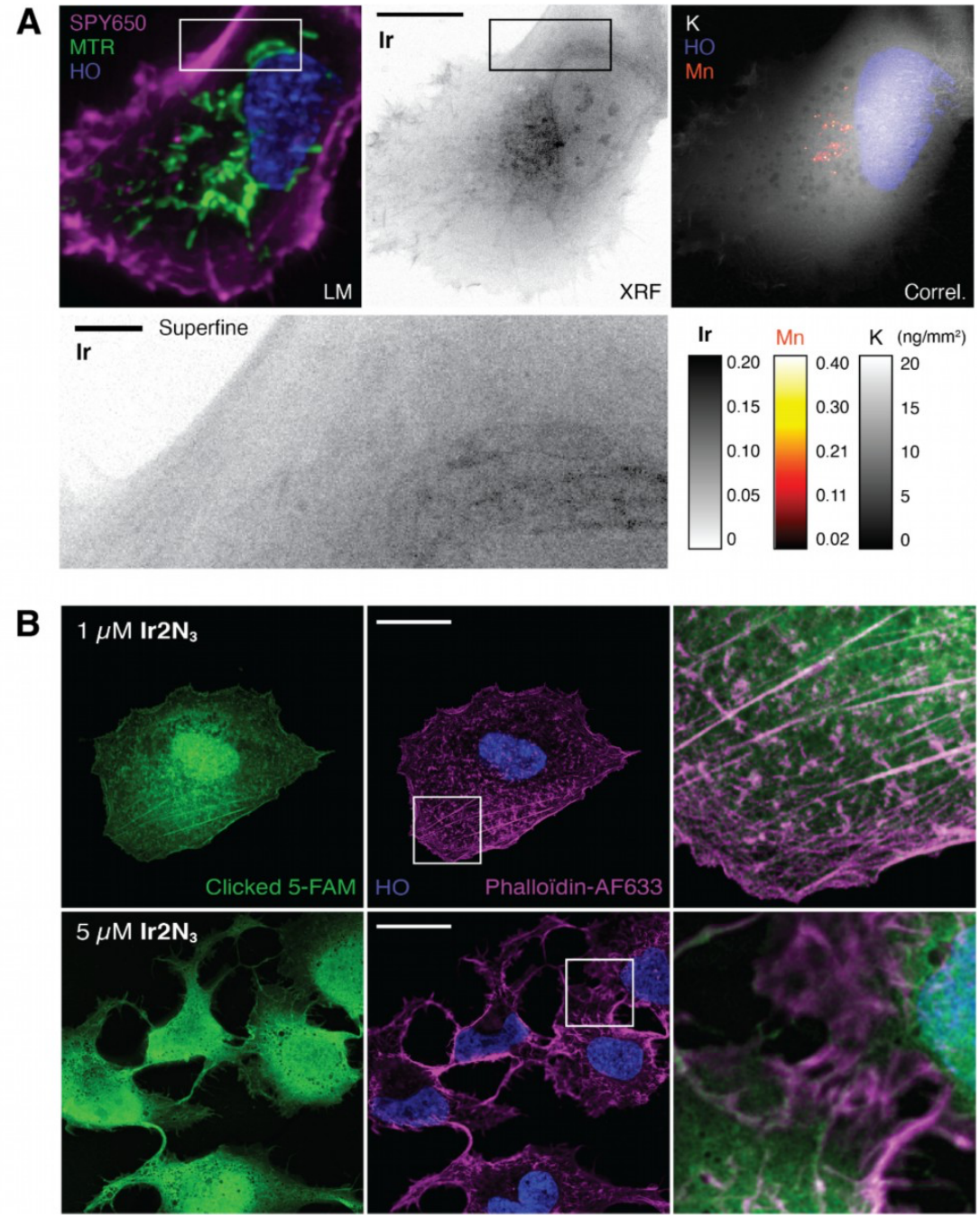

Figure 4. High resolution imaging techniques reveal a pan-cellular distribution of Ir2 and Ir2N$_3$

(**A**) Correlative analysis of a frozen-hydrated hTERT-RPE1 cell treated with 5 µM **Ir2** for 15 min and imaged at 88 K. Light cryomicroscopy (LM) of the actin cytoskeleton (SPY650-Fast Act, magenta), mitochondria (Mitotracker Green, MTR) and the nucleus (Hoechst 33342, blue, HO). Cryo-X-Ray Fluorescence imaging (XRF) of elemental Ir, Mn and K expressed in ng/mm^2 as color-scales of Amber, Fire and Gray respectively, acquired at 50 nm/px/50 ms or "superfine" 30 nm/px/100 ms resolution. Scale bars: 10 and 1 µm.

(**B**) Super-resolution confocal images of Huh-7 cells exposed to **Ir2N$_3$** for 1 h (top 1 µM, bottom 5 µM), fixed and clicked *in situ* with FAM alkyne (green). Staining of actin cytoskeleton (phalloidin, magenta) and DNA (Hoechst 33342, blue). Zoom on a selected region of 200 µm^2 showing colocalization of **Ir2N$_3$** and microfilaments (white) on the merged images. Scale bar: 20 µm.

Quantitation of iridium in the whole cell shown in **Figure 4A** led to an estimate of 70 fg consistent with the ICP-OES bulk analysis performed in parallel, giving an iridium content of 130 ± 2 fg per cell.

Click-based imaging of $Ir2N_3$ validates the actin cytoskeleton and the molecular chaperone Heat Shock Protein 90 (HSP90) as intracellular targets

Taking advantage of the bioorthogonal azido function carried by **$Ir2N_3$**, its intracellular distribution was also analyzed using in-cell labeling by click chemistry[43] with a fluorophore introduced in fixed samples, once the complex has reached its intracellular biological targets (*in situ*). Using this approach, only the strongly bound and chemically accessible iridium complex pool and not the free and therefore diffusible one should be observed by fluorescence microscopy. Both complexes **IrN_3** and **$Ir2N_3$** clicked to the ethynyl-substituted derivative of fluorescein (FAM alkyne) displayed a constant staining pattern at various concentrations and were detectable from 15 min post treatment. The acquired images are consistent with the XRF data described above, supporting that **$Ir2N_3$** and **IrN_3** (**Figure 4B** and **Figure S8B**) are detectable using in-cell click chemistry in both the nucleus and cytoplasm. Notably, clicked iridium complexes co-localized with the actin cytoskeleton and perturbed these fibers in a dose-dependent manner. Stress fibers (large contractile filaments of actin and myosin) identified with fluorescent phalloidin, were stained at low concentration of **$Ir2N_3$** with FAM alkyne as shown in **Figure 4B**. At concentrations of complexes around the IC_{50}, they were not detectable and the cortical actin network appeared diffuse and disorganized, indicating that actin cytoskeleton with its associated proteins is a key target of the tested iridium compounds, in full agreement with the presence of relevant actin-binding proteins in the chemoproteomic analysis.

In order to probe the interaction of **$Ir2N_3$** with several protein targets representative of predominant molecular functions identified in our GO term analysis, we introduced a proximity ligation assay (PLA) in which **$Ir2N_3$** was clicked to biotin and the protein target of interest was labeled with a specific primary antibody. Then PLA was performed using selective oligonucleotide-labeled antibodies to biotin and the primary antibody (**Figure S9**). Strong and dose-dependent PLA signals

were obtained with the chaperone HSP90 and the actin-binding protein Filamin B (FLB), belonging to the group of **Ir2N$_3$** "high affinity" targets (**Figure 5A)**. Two proteins with similar functions, the chaperone GRP78 (intermediate affinity) and the actin-binding protein Arp2/3 (absent from the iridium interactome), gave little to no PLA signal after **Ir2N$_3$** treatment. We thus conclude that HSP90 and Filamin B are preferred **Ir2N$_3$** protein targets in hTERT-RPE1 cells as well.

Folding activity of the chaperone HSP90 is inhibited by Ir2

The dose-dependent effect of **Ir2** on the activity of two chaperones identified as high affinity targets, HSP90 and HSP70 (encoded by HSP90B1 and HSPA1B, respectively), was also probed by two functional *in vitro* assays to monitor their ATPase and ATP-dependent foldase activities. The latter was quantified on a model luciferase substrate using a reconstituted chaperone system composed of HSP90, HSP70 and their respective cochaperones STIP1 and DNAJB1. Although we observed a moderate increase of HSP90 ATPase activity after **Ir2** treatment (**Figure 5B**), we found that **Ir2** strongly inhibited HSP90 capacity to refold luciferase (**Figure 5C**). We used a similar approach to probe the activities of HSP70 upon **Ir2** treatment and first observed a moderate inhibition of its ATPase activity by **Ir2**. However, when we added to the assay DNAJB1, an HSP40 cochaperone needed for HSP70 chaperone function and accelerating its ATPase activity, we observed a stronger response to the cochaperone stimulation of HSP70 when treated with **Ir2** compared to DMSO (**Figure S10A)**. We also looked at the refolding capacity of HSP70 on denatured luciferase and observed no difference in the foldase activity upon treatment with **Ir2** or DMSO vehicle (**Figure S10B**). Overall, we conclude that while **Ir2** binds to both HSP90 and HSP70 with high efficiency, only HSP90 chaperone activity appears affected *in vitro*. **Ir2** most probably alters HSP90 ability to recognize its client protein substrates without interfering with its ATPase activity and hence its overall structure.

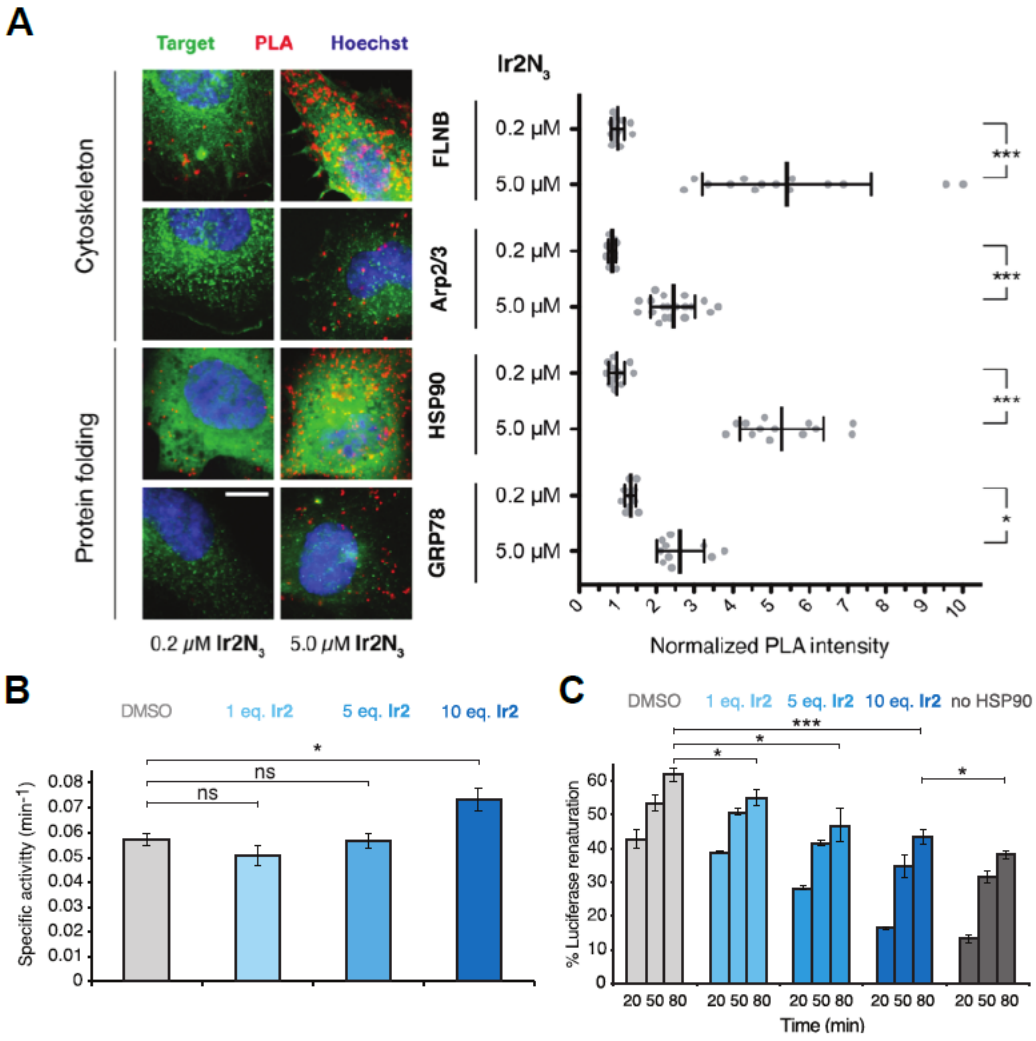

Figure 5. Cellular and functional *in vitro* assays validate Filamin B and HSP90 as *bona fide* intracellular targets of iridium compounds

(**A**) Quantification of the PLA signal in hTERT-RPE1 cells treated with **Ir2N$_3$** for 15 min at the two indicated concentrations. Representative images of the PLA signal (red) and co-immunofluorescence of the protein target (green), DNA stained with Hoechst 33342 (blue). Scale bar: 5 µm. PLA signal intensity per cell (N = 10 – 20) was normalized using a control condition with the target-antibody alone. Statistical significance was calculated using one-way analysis of variance with a Bonferroni post-test (*$p < 0.05$; ***$p < 0.001$).

(**B**) Specific ATPase activity of HSP90, either treated with DMSO vehicle (light grey) or with 1 (light blue), 5 (medium blue) or 10 (dark blue) molar equivalents of **Ir2**, given as mean of three replicates ± SD. Student's t-test was used to determine the statistical significance of differences observed between **Ir2**- and DMSO-treated samples (ns not significant; *$p < 0.05$; ***$p < 0.001$).

(**C**) HSP90 foldase activity reported as the percentage of luciferase renaturation after 20, 50 or 80 min of incubation in a reconstituted chaperone system with HSP90, either treated with DMSO vehicle (light grey) or with 1 (light blue), 5 (medium blue) or 10 (dark blue) molar equivalents of **Ir2**, or in the absence of HSP90 (dark grey). Results are expressed as mean of three replicates ± SD. Student's t-test was used to determine the statistical significance of differences observed at 80 min of incubation (*$p < 0.05$; ***$p < 0.001$). Statistical analysis performed at all time points is detailed in **Figure S11**.

Ir2N$_3$ disorganizes the cytoskeleton and impairs cell adhesion

We previously observed that cellular motility is rapidly abolished upon treatment with half-sandwich iridium complexes including **Ir2.**[13] Dose-dependent effects of both **IrN$_3$** and **Ir2N$_3$** observed on cell motility (**Supplemental video 1**) and the actin cytoskeleton (**Figure 4B**), together with our finding of numerous microfilament-associated proteins amongst **Ir2N$_3$** high affinity targets, prompted us to further investigate the dynamics of actin filaments. Near-diploid hTERT-RPE1 cells were chosen for this analysis as they exhibit a non-transformed phenotype with an unperturbed actin meshwork.[44] Time-lapse videomicroscopy of the actin cytoskeleton was performed using a fluorescent probe (SPY650-FastAct). Complete inhibition of the exploratory phenotype was observed in hTERT-RPE1 cells upon **Ir2** treatment, in contrast to control cells displaying highly dynamic lamellipodia and filopodia (**Supplemental video 2**). The assembly of new actin microfilaments was inhibited immediately after addition of 5 μM **Ir2**, followed by the complete disappearance of large structures (stress fibers) after *ca.* 60 min. Condensation of the fluorescent signal in patches suggested aggregation of shorter microfilaments that accumulated close to the plasma membrane.

Alterations of the cytoskeleton at the nanometer scale were further examined by correlative light and scanning electron microscopy (CLSEM) on cells seeded on fibronectin-coated micropatterns to constrain cellular architecture. This method allows a highly reproducible analysis of cell morphology and facilitates correlative microscopy.[45,46]

To expose cytoskeletal structures and more generally reveal the topography of non-membranous internal structures before CLSEM acquisitions, hTERT-RPE1 cells exposed or not to 10 μM **Ir2N$_3$** for 15 min were extracted with a detergent prior to fixation by dissolving the plasma membrane and removing soluble particles. During this step, a fluorescent phalloidin was employed both to stabilize the actin microfilaments and stain the network, then **Ir2N$_3$** was labeled using FAM alkyne. Under these conditions, the intracellular distribution of **Ir2N$_3$** was unaffected, showing a reproducible colocalization with microfilaments. According to the micrographs, the cytoskeleton of

treated cells appears less dense and less organized compared to control cells (**Figure 6A**). Disorganization of cytoskeleton in treated cells was quantified using a directionality analysis (**Figure 6B**) of cells constrained on disc micropatterns, demonstrating that **Ir2N$_3$** disrupts cytoskeletal organization after only 15 min of incubation.

Alterations of the actin cytoskeleton can result from perturbation of the actin monomer *per se* and its intrinsic ability to polymerize/depolymerize but also of the dynamic interaction of actin monomers and microfilaments with actin-binding proteins. Our chemoproteomic results point to the latter hypothesis as only actin regulators were identified in the iridium interactome, but not actin itself. To rule out any possible direct interference of **Ir2N$_3$** with actin polymerization/depolymerization properties, *in vitro* assays were performed. Actin monomer polymerization into microfilaments was not prevented in the presence of 1 or 10 equivalents of **Ir2N$_3$** (data not shown). Likewise, the polymers remained stable in the presence of **Ir2N$_3$**. We thus conclude that actin cytoskeleton alterations in the presence of **Ir2**/**Ir2N$_3$** exclusively arise from their interaction with actin-binding proteins and cross-linkers responsible for the integrity of the cytoskeletal meshwork.

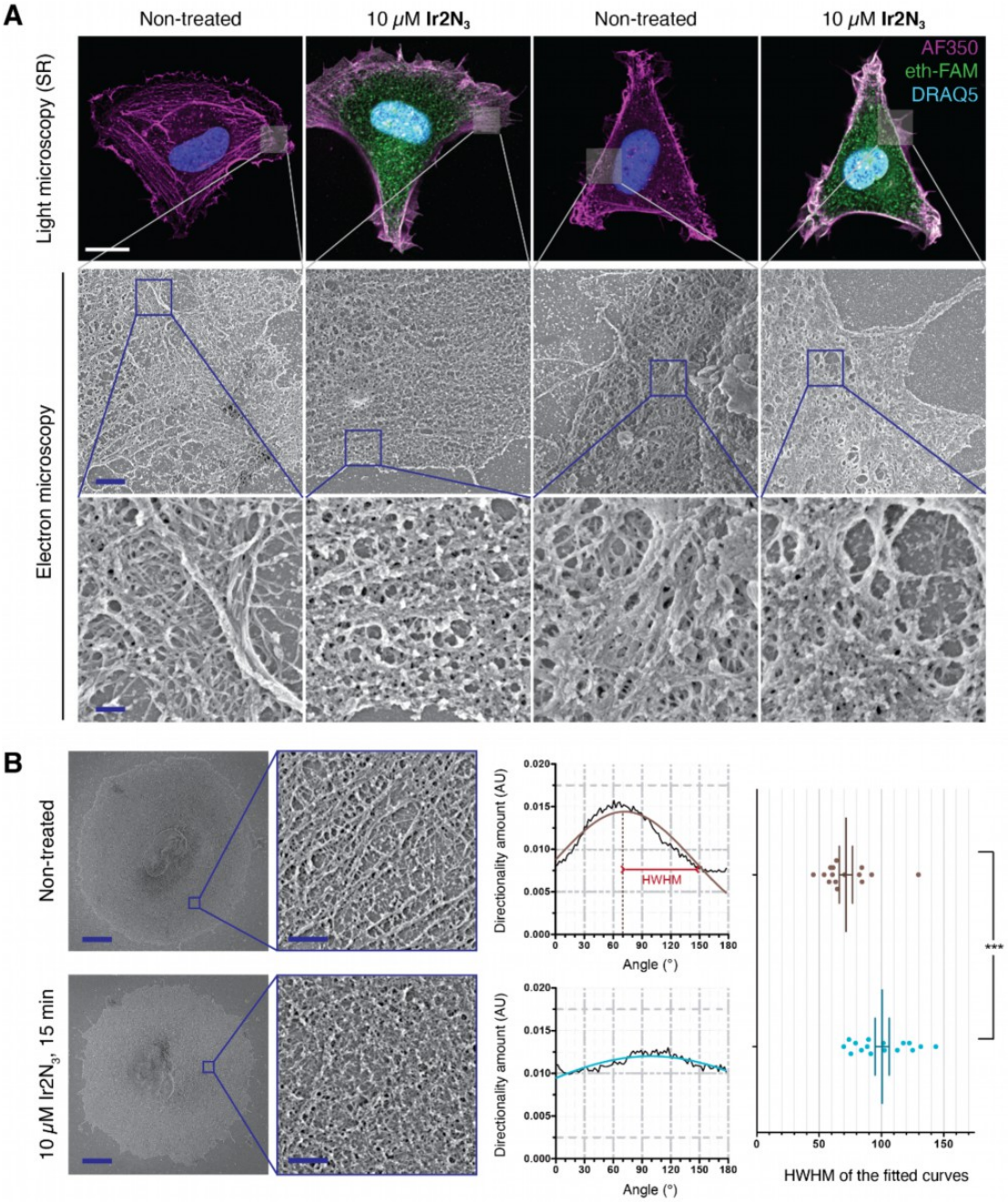

Figure 6. $Ir2N_3$ induces a dramatic disorganization of the cytoskeletal meshwork

(**A**) Multiscale analysis by Correlative Light and Scanning Electron Microscopy. Cells were seeded on crossbow or arrowhead-shaped fibronectin-coated micropatterns, treated for 15 min with **$Ir2N_3$** or vehicle alone, then extracted with detergent prior to fixation. Labelling of **$Ir2N_3$** (FAM alkyne, green), microfilaments (AlexaFluor-350 phalloidin, magenta) and DNA (DRAQ5, blue), detected by super-resolution confocal microscopy. Correlative scanning electron microscopy. Scale bars: 10 µm, 1 µm, 200 nm respectively.

(**B**) Cytoskeletal organization of extracted cells seeded on disc-shaped micropatterns of 42 µm diameter. Scale bars: 5 µm, 500 nm. Directionality analysis was performed over 15 – 16 cropped squares in the cortical region of 10 cells per condition. For each image, directionality of cytoskeletal filamentous structures was analyzed using local gradient orientation for each considered angle. The half-width at half-maximum (HWHM) of each fitted gaussian are compared for the treated and control conditions. Statistical significance was calculated using a two-tailed t-test (p = 0.0009, ***).

Discussion and Conclusions

The first cytotoxic half-sandwich iridium(III) complexes have been introduced ten years ago[10,47] and have since continuously attracted interest, mostly owing to a mode of action different from platinum complexes. These antiproliferative properties were demonstrated on cancer cell cultures including platinum-resistant cell lines, as well as on solid tumors.[6,48–50] Most complexes reported in the literature are known to increase reactive oxygen species (ROS) levels in cells[12,13,16,51] and induce mitochondrial uncoupling,[52] triggering apoptotic cell death. Consistently, upregulation of the antioxidant response was demonstrated in a pharmaco-genomic study realized in ovarian cells treated with a highly active azopyridine iridium complex.[34] Both iridium complexes **Ir2** and **Ir2N$_3$** reported herein show a similar behavior as they rapidly increase H_2O_2 intracellular levels, prompting the activation of the transcription factor Nrf2 as a response to oxidative stress. This pro-oxidant property accounts for the antiproliferative activity of these molecules on cancer cells and more generally of metal-based drug candidates.[53] However, iridium complexes with poor pro-oxidant catalytic ability, such as **Ir1**[13] and **IrN$_3$**, are nonetheless cytotoxic.

Metal complexes including labile ligands can also be viewed as electrophiles able to react with a variety of intracellular nucleophiles to form covalent adducts. Some half-sandwich iridium complexes were shown to form adducts with the model nucleobase 9-ethylguanine *in vitro*.[54,55] Indeed, **Ir2N$_3$** was readily detected in the nucleus, in agreement with the XRF results for **Ir2** and consistent with our detection of nuclear proteins in the iridium interactome. However, the absence of DNA damage in **Ir2** treated cells and the absence of a detectable interaction between **Ir2** and DNA *in vitro* both argue against a possible binding of **Ir2** with nuclear DNA *in vivo*. **Ir2** was also detected in mitochondria by XRF, consistent with our observation that increasing concentrations of **Ir2** altered mitochondria morphology and membrane potential, also in agreement with others.[16,56]

Here, formation of covalent adducts between **IrN$_3$** or **Ir2N$_3$** and cellular proteins *in vivo* was unequivocally demonstrated and allowed us to profile these targets by click-based chemoproteomics.

Amongst the 211 high affinity and 20 most enriched targets of **Ir2N$_3$**, we identified filamin A and B, the latter exhibiting the lowest p-value. We further demonstrated the relevance of this protein target by proximity ligation assay. Filamin A/B are essential to actin filaments crosslinking and cytoskeletal remodeling during cell adhesion and migration. We thus propose that **Ir2** strongly interferes with filamins and/or other actin binding proteins identified in our screen, accounting for the phenotype of iridium-treated cells. Disorganization of the cytoskeleton architecture was confirmed by high-resolution imaging approaches and quantified at the nanometer scale by scanning electron microscopy. At the cellular level, cell adhesion and motility were greatly perturbed, presumably leading to anoikis-induced apoptosis.[57]

A correlation between drug intracellular concentration and drug toxicity is widely documented. It was initially suggested by Sadler *et al.* while studying (C^N) and (N^N)-chelated isoelectronic half-sandwich iridium complexes[10] and more recently by Pizarro *et al.*[16] In this study, after 30 min incubation with 5 µM **Ir2** in the extracellular medium, we measured an intracellular concentration of 570 µM elemental iridium by ICP-OES, based on a mean HeLa cell volume of 3700 µm^3. This 100-fold concentration ratio indicates that HeLa cells display a typical "sponge-like" behavior[58] toward **Ir2**, *i.e.* displacement of the in/out equilibrium of the free molecule, most likely driven by the formation of intracellular covalent adducts. While this effect may have favored catalytic production of H_2O_2 and therefore toxicity in HeLa cells, the measured intracellular concentration of elemental iridium in hTERT-RPE1 cells was 4 times lower. This striking discrepancy between cell lines provides a possible explanation for the observed threshold effect on cell proliferation, monitored by RTCA.

Formation of covalent adducts can have diverse consequences on protein function, through conformational changes, hindering of protein-protein interaction and inhibition of enzyme catalytic function. We found several chaperones amongst the high affinity proteins targets of **Ir2N$_3$**, including the Heat Shock Proteins 90 and 70. We used these HSPs as a paradigm to investigate the effects of iridium adducts on their catalytic ATPase activity, specific protein-protein interaction, and folding

capacity. Our results showed contrasting effects of **Ir2** on these chaperones. Indeed, HSP90 ATP-dependent chaperone activity was strongly inhibited by **Ir2**, almost abolishing its capacity to refold a model substrate at **Ir2** concentrations similar to those reached in cells, while leaving its ATPase activity unaffected. In contrast, treatment of HSP70 by **Ir2** strengthened its capacity to be stimulated by its cognate cochaperone DNAJB1 (Hdj1) leading to an increased ATPase activity with an equal capacity to refold a model substrate *in vitro*. These results revealed distinct modes of action on the two HSPs and indicate that **Ir2** does not necessarily inhibit target protein function.

In conclusion, the cytotoxic effect of **Ir2** and its congeners appears to arise from their ability to accumulate in cells by passive diffusion and induce both oxidative stress and formation of covalent adducts with a subset of proteins, as a consequence of their dual chemical reactivity. Herein, we reported the first comprehensive list of protein targets of a half-sandwich iridium complex and clues to understand the mechanisms underlying its cytotoxicity from the molecular to the cellular levels. Besides, by combining proteomics, imaging, cell biology and biochemistry, we established explicit links between complex accumulation, subcellular distribution, protein targets and cellular response. One of the main hallmarks of cancer is cytoskeletal rearrangement initiated during epithelial-mesenchymal transition that drives metastasis onset. Another feature of some cancer cell types is their higher sensitivity to ROS accumulation[59] or their higher dependency upon molecular chaperones[60]. In this context, **Ir2** provides a unique combination by targeting cytoskeletal and chaperone proteins in direct relation with cancer progression and by triggering ROS production to selectively elicit cancer cell death. Future approaches will be needed to challenge these various aspects on animal models of tumorigenesis and metastasis.

Experimental Section

Synthetic procedures and compound characterization

Reagents were purchased as reagent-grade and used without further purification. 2-(4-(chloromethyl)phenyl)-4,5-dihydrooxazole and **Ir2** were synthesized according to the literature procedure.[13] Dichloro(pentamethylcyclopentadienyl)iridium(III) dimer was purchased from Strem Chemicals. All reactions were monitored by analytical TLC on silica gel 60 F254 plates 0.25 mm, and visualized under UV light (λ = 254 and 365 nm). Silica gel (SDS 60 ACC 35–70 mm) or alumina (90 basic, Macherey-Nagel) was used for column chromatography. NMR spectra were recorded on Bruker Avance III 300 MHz or 400 MHz spectrometers. Chemical shifts (δ) are expressed in part per million (ppm), reported as s = singlet, d = doublet, t = triplet, m = multiplet; and referenced to the solvent peak of respectively $CDCl_3$, CD_2Cl_2 (^{13}C NMR: δ = 77.23; 53.84 ppm; ^1H NMR: δ = 7.26; 5.32 ppm). ESI-HRMS analysis were carried out using an LTQ-Orbitrap XL from Thermo Scientific (Thermo Fisher Scientific, Courtaboeuf, France) and operated in positive ionization mode. IR spectra were recorded on a FT-IR spectrometer (Tensor 27, Bruker) equipped with an ATR MIRacle (Pike Technologies) accessory. All new compounds are > 95% pure by HPLC except **IrN$_3$** (93%).

2-(4-(azidomethyl)phenyl)-4,5-dihydrooxazole

2-(4-(chloromethyl)phenyl)-4,5-dihydrooxazole (0.5 g, 2.55 mmol) was dissolved in MeCN (20 mL) and DMF (1 mL) was added. NaN_3 (0.25 g, 1.5 equiv.) was added to the stirred solution that was refluxed for 16 h. The reaction mixture was treated with water (20 mL) and the aqueous layer was extracted three times with dichloromethane. The organic layers were washed three times with H_2O, dried over magnesium sulfate, filtered and evaporated to give a yellow oil. It was dissolved in Et_2O and washed three times with brine. After drying with magnesium sulfate, filtering and removing the solvent, a yellowish oil was obtained again that turned into a solid (466 mg, 90%) after complete drying. ^1H NMR (300 MHz, $CDCl_3$) δ (ppm) 7.96 (dd, 2H, *J* = 6.6, 1.8 Hz, H3), 7.35 (dd, 2H, *J* = 6.6, 1.8 Hz, H2), 4.44 (t, 2H, J = 9.5 Hz, H7), 4.39 (s, 2H, H8), 4.07 (t, 2H, J = 9.5 Hz, H6). ^{13}C {^1H} NMR

(75 MHz, $CDCl_3$) δ (ppm): 164.3 (C5), 138.7 (C4), 128.8 (C3), 128.1 (C2), 127.9 (C1), 67.8 (C7), 55.1 (C6), 54.5 (C8). IR (ATR): ν(N=N=N) = 2081 cm^{-1}.

Chlorido(η5-pentamethylcyclopentadienyl)(2-((4-azidomethyl)phenyl-κC2)-4,5-dihydrooxazole-κN)Iridium(III) (IrN_3)

Anhydrous dichloromethane (10 mL) was degassed for 15 min over 4 Å MS and dichloro(pentamethylcyclopentadienyl)iridium(III) dimer (204 mg, 256 µmol, 1.0 equiv.) was dissolved into the mixture. Activated AcONa (126 mg, 1.537 mmol, 6.0 equiv.) was added to the stirred solution and 2-(4-(azidomethyl)phenyl)-4,5-dihydrooxazole (109 mg, 539 µmol, 2.2 eq.) was added after 90 min stirring under argon atmosphere. The reaction was stirred 1 h at room temperature and became orange, it was filtered over a pad of dry Celite® 545 and evaporated to a semi-solid foam. This crude product was washed twice with pentane and dissolved in dichloromethane (3 mL), excess pentane was added and red precipitate containing mostly impurities were formed. The filtrate was a yellow solution from which part of the pure product could be crystallized by slow evaporation from a concentrated solution in dichloromethane (one week) to yield pure orange crystals (62 mg, 8%). ^1H NMR (300 MHz, CD_2Cl_2) δ (ppm) 7.72 (s, 1H, H2), 7.41 (d, 1H, *J* = 7.7 Hz, H5), 6.97 (dd, 1H, *J* = 7.7, 1.3 Hz, H4), 4.93 – 4.76 (m, 2H, H9), 4.46 (d, 1H, *J* = 13.6 Hz, H10a), 4.36 (d, 1H, *J* = 13.6 Hz, H10b), 4.10 (ddd, 1H, *J* = 12.5, 9.7, 7.8 Hz, H8a), 3.91 (ddd, 1H, *J* = 12.5, 10.6, 9.2 Hz, H8b), 1.76 (s, 15H, HCp*). ^{13}C {^1H} NMR (75 MHz, CD_2Cl_2) δ (ppm) 180.0 (C1), 165.5 (C7), 139.2 (C3), 135.8 (C2), 131.6 (C6), 126.7 (C4), 122.1 (C5), 88.3 (CCp*), 72.2 (C9), 55.7 (C8), 50.8 (C10), 9.6 (CH_3Cp*). HRMS (ESI+): m/z calculated for $C_{20}H_{24}ClIrN_4O$: 529.1574; found: 529.1574 $[M-Cl]^+$. IR (ATR): ν(N=N=N) = 2091 cm^{-1}.

4,4-dimethyl-2-(4-(chloromethyl)phenyl)-4,5-dihydrooxazole

To a stirred solution of 4-(chloromethyl)benzoyl chloride (1.046 g, 5.53 mmol) in dichloromethane (30 mL), 2-amino-2-methyl-1-propanol (1.233 g, 2.5 eq, 13.83 mmol) was added portion wise and the reaction was stirred for 1 h. H_2O (10 mL) was added to the mixture and the aqueous layer was extracted

three times with ethyl acetate. Organic layers were dried over magnesium sulfate and evaporated to give 1.410 g of a white powder. This intermediate product was dissolved in dichloromethane (20 mL) and a large excess of thionyl chloride (1.7 mL, 4.0 equiv.) was added dropwise. The solution was stirred at room temperature overnight. The suspension was poured over ice and the aqueous layer was neutralized with solid sodium bicarbonate (10 g). The neutral aqueous layer was then extracted 3 times with ethyl acetate and the combined organic layers were washed with water, dried over magnesium sulfate and evaporated to give a colorless oil. The resulting crude product was dissolved in 25 mL of THF and 60% NaH in mineral oil (332 mg, 1.5 equiv.) were added portionwise. The resulting brown reaction mixture was stirred for 2 h at room temperature. The reaction was quenched with a saturated aqueous ammonium chloride solution. The mixture was decanted and the aqueous layer was extracted three times with dichloromethane. The combined organic layers were washed with water, dried over solid magnesium sulfate, filtered and evaporated to give a crude yellow semi-solid product (1.211 g, 90%). ^{1}H NMR (400 MHz, CD_2Cl_2) δ (ppm): 7.90 (d, *J* = 8.3 Hz, 2H, H2), 7.43 (d, *J* = 8.7 Hz, 2H, H3), 4.63 (s, 2H, H8), 4.10 (s, 2H, H7), 1.34 (s, 6H, HMe2). ^{13}C {^{1}H} NMR (101 MHz, CD_2Cl_2) δ (ppm): 161.6 (C5), 141.0 (C4), 129.0 (3C, C1, C2, C3), 79.6 (C7), 68.2 (C6), 46.3 (C8), 28.7 (CMe_2). HRMS (ESI+): m/z calculated for $C_{12}H_{14}ClNOH$: 224.0837; found: 224.0838 $[M+H]^+$ (+0.6 ppm).

4,4-dimethyl-2-(4-(azidomethyl)phenyl)-4,5-dihydrooxazole

Crude 4,4-dimethyl-2-(4-(chloromethyl)phenyl)-4,5-dihydrooxazole was dissolved in acetonitrile (10 mL) containing dimethylformamide (0.5 mL). Sodium azide (100 mg, 1.7 equiv.) was added and the reaction mixture was refluxed during 14 h. H_2O (10 mL) was added to the mixture and the aqueous layer was extracted twice with dichloromethane. The organic layers were washed twice with water, dried over magnesium sulfate, and evaporated in vacuo to give a colorless oil (173 mg, 82%). ^{1}H NMR (400 MHz, CD_2Cl_2) δ (ppm): 7.92 (d, *J* = 8.3 Hz, 2H, H2), 7.37 (d, *J* = 8.6 Hz, 2H, H3), 4.40 (s, 2H, H8), 4.10 (s, 2H, H7), 1.34 (s, 6H, HMe2). ^{13}C {^{1}H} NMR (101 MHz, CD_2Cl_2) δ (ppm): 161.7 (C5),

139.1 (C4), 129.0 (C3), 128.8 (C1), 128.5 (C2), 79.7 (C7), 68.2 (C6), 54.9 (C8), 28.7 (CMe_2). HRMS (ESI+): m/z calculated for $C_{12}H_{14}N_4OH$: 231.1240; found: 231.1242 $[M+H]^+$ (+0.7 ppm).

Chlorido(η5-pentamethylcyclopentadienyl)(2-((4-azidomethyl)phenyl-κC2)-4,5-dihydro-2,2-dimethyloxazole-κN)Iridium (III) (Ir2N$_3$)

Dichloro(pentamethylcyclopentadienyl)iridium(III) dimer (726 mg) was dissolved in dichloromethane (50 mL) and sodium acetate (448 mg, 6.0 eq, mortar, anhydrous) was added to the red solution. The mixture was stirred at room temperature in the dark during 2 h, by which it turned to orange. 4,4-Dimethyl-2-(4-(azidomethyl)phenyl)-4,5-dihydrooxazole (2.2 equiv., 456 mg) dissolved in dichloromethane (3 mL) was added and the mixture quickly turned brown and was stirred at room temperature for 45 min. The suspension was filtered over a pad of Celite® 545 and the filtrate evaporated to give a residue which was triturated with cyclohexane. The resulting solid was redissolved in dichloromethane (3 mL) and cyclohexane (60 mL) was added to the solution. The resulting red precipitate was discarded and the filtrate was evaporated to give ca. 750 mg of crude product. This crude product containing a mixture of ligand and complex in 45/55 ratio was purified over neutral alumina using cyclohexane/AcOEt (9:1) as eluant. Crystallization by slow evaporation gave **Ir2N$_3$** as a yellow powder (150 mg, 14%). ^{1}H NMR (400 MHz, CD_2Cl_2) δ (ppm) 7.70 (d, *J* = 1.6 Hz, 1H, H2), 7.42 (d, *J* = 7.7 Hz, 1H, H5), 6.96 (dd, *J* = 7.8, 1.6 Hz, 1H, H4), 4.56 – 4.34 (m, 4H, H9,H10), 1.77 (s, 15H, HCp*), 1.49 (2s, 6H, HMe2). ^{13}C {^{1}H} NMR (101 MHz, CD_2Cl_2) δ (ppm): 177.8 (C1), 164.2 (C7), 139.1 (C3), 135.6 (C2), 133.1 (C6), 126.6 (C4), 122.1 (C5), 88.6 (CCp*), 83.5 (C9), 68.1 (C8), 55.8 (C10), 28.8 (CMe_2), 26.6 (CMe_2), 10.2 (CH_3 Cp*). HRMS (ESI+): m/z calculated for $C_{22}H_{28}IrN_4O$: 557.1887; found 557.1887 $[M-Cl]^+$ (0.0 ppm).

[Dimethylsulfoxide-(η5-pentamethylcyclopentadienyl)(2-phenyl-κC2-(4-dimethyl)oxazoline-κN)Iridium (III)] Hexafluorophosphate (Ir2-DMSO)

Ir2 (200 mg, 372 µmol) was dissolved in 5 mL of dichloromethane and 5 mL of MeOH/H_2O (1:1) were added. Another 10 mL of methanol were added to obtain one homogeneous layer. Silver nitrate

(69.5 mg, 409 µmol, 1.1 equiv.) was poured into the solution and a white precipitate immediately appeared. The solution was left stirring for 1 h. DMSO (26.4 µL, 372 µmol, 1.0 equiv.) was added and the solution turned from golden to pale yellow. Stirring continued for 5 min and NH_4PF_6 (339 mg, 2.08 mmol, 5.6 equiv.) was added. After 15 min, the crude mixture was filtered through a sintered glass frit (Porosity 3 equipped with paper filter) and the filtrate was evaporated. The obtained suspension was redissolved in dichloromethane and the solution was washed with H_2O to remove excess NH_4PF_6. The product was isolated from the organic phases, after drying with $MgSO_4$ and evaporating volatiles, as a pale-yellow solid (271 mg, 99%). A single monocrystal suitable for X-Ray diffraction analysis was obtained from a concentrated MeOH solution. ^{1}H NMR (400 MHz, MeOD) δ (ppm): 7.71 (d, *J* = 7.6 Hz, 1H, H2), 7.59 (dd, *J* = 7.6, 1.5 Hz, 1H, H5), 7.44 (td, *J* = 7.5, 1.5 Hz, 1H, H4), 7.29 (td, *J* = 7.5, 1.0 Hz, 1H, H3), 4.83 (d, *J* = 8.9 Hz, 1H, H9), 4.67 (d, *J* = 8.9 Hz, 1H, H9), 3.22 (s, 3H, DMSO), 2.53 (s, 3H, DMSO), 1.90 (s, 15H, HCp*), 1.59 (s, 3H, H10), 1.51 (s, 3H, H10). ^{13}C {^{1}H} NMR (101 MHz, MeOD) δ (ppm): 191.0 (C1), 143.0.7 (C7), 133.2 (C6), 135.5 (CAr), 133.9 (CAr), 127.9 (CAr), 124.5 (CAr), 116.4 (C8) 96.7 (CCp*), 83.1 (C9), 45.7 (CH_3 DMSO), 45.6 (CH_3 DMSO), 28.2 (C10), 24.8 (C10), -8.7 (CH_3 Cp*).

HPLC analysis

HPLC analysis was performed using a HPLC system (Jasco) comprising PU-2080 and PU-2087 pumps coupled to a uv-visible detector (UV-2075). Separations were performed on a 4.6 x 150 mm Nucleodur C18 5 µm column (Macherey-Nagel).

Partition coefficient (log P) determination

The partition coefficient (log $P_{o/w}$) of the complexes was determined by an HPLC method according to the Test guideline no. 117 recommended by OEDC,[33] using a series of seven reference substrates (Benzonitrile, Anisole, Toluene, Naphthalene, Diphenyl ether, n-butylbenzene, Triphenylamine). Elution conditions were 70 % MeCN – 30 % 10 mM ammonium acetate in water at a flow rate of 1 ml/min, detection set at 254 nm.

ICP-OES analysis

100-mm culture dishes were seeded with $1x10^6$ HeLa cells in complete medium. After two days, the medium was replaced by 10 mL of low glucose, serum-free DMEM and cells were incubated at 37°C under 5% CO_2. After 30 min, a pretreatment step was conducted by adding 20 µM CCCP and/or 50 mM 2-DG followed by another 30 min incubation. Subsequently, cells were treated with 4 µM **Ir2** and incubated for 30 min. After treatments, supernatants were carefully collected. Cells were washed with PBS, detached by trypsin, resuspended in serum-free DMEM, counted and pelleted by centrifugation at 200 g. Prior to ICP analysis, HNO_3 was added to the supernatants to reach a final concentration of 2 wt%. Cell pellets were resuspended in 0.15 mL of 68 wt% HNO_3 and sonicated using a sonication probe 3 times for 10 seconds. The volume was then adjusted to 7 mL with ultrapure water to achieve a final concentration of 2 wt% HNO_3. Determination of iridium concentration in cell samples was performed on an ICP-OES 5100 SVDV analyzer (Agilent). Iridium calibration standards (5 – 1000 ppb in 2% HNO_3) were prepared from a 10 ppm PlasmaCAL SCP Science® multi-element stock solution. Measurements were performed in triplicate.

Cell culture

HeLa, HEK-293, A2780, hTERT-RPE1 and Huh-7 were authenticated using short tandem repeat profiling and routinely tested for the absence of mycoplasma contamination. HeLa (human cervix carcinoma), HEK293 (human embryonic kidney) and A2780 cells were cultured in DMEM High Glucose. hTERT RPE1 cell line was cultured in DMEM/F12 supplemented with 15 mM HEPES. Huh-7 was cultured in Minimum Essential Medium (MEM) supplemented with 1 % sodium pyruvate and 1 % non-essential amino acids (Gibco, Invitrogen). All media were supplemented with GlutaMAX (Gibco, Invitrogen), antibiotics (penicillin, streptomycin) and 10 % fetal bovine serum, and are further referred to complete medium. All short treatments with **Ir2**, **IrN_3**, **$Ir2N_3$** were performed in serum-free media and treatments longer than 3 h were performed in medium containing 5% FBS.

HeLa cell spheroids

500 HeLa cells were seeded into each well of a low binding 96-well plate with round bottom, with a final volume of 200 µL of complete medium. The plate was then centrifuged at 120g for 4 minutes and incubated at 37°C under 5% CO_2. After 6 h, cells were treated with **Ir2** by replacing 100 µL of medium with an equivalent volume of serum-free medium containing the desired concentration of **Ir2**. Spheroid development was continuously monitored during the incubation period. After 6 days, spheroids were imaged and their surface was measured using Fiji. For alamarBlue analysis, 100 µL of medium was replaced with an equivalent volume of serum-free medium containing 100 µM of alamarBlue. Following 4 h of incubation, 100 µL was transferred into a new 96-well plate with transparent and flat bottoms, and fluorescence was measured with excitation at 540 nm and emission at 590 nm.

Cell viability assays

Stock solutions of **Ir2** (10 mM), **Ir2N$_3$** and **IrN$_3$** (20 mM) were prepared in DMSO and incubated 24 h at room temperature before storage, to allow complete chlorido to DMSO ligand exchange (Fig. S1B). 4,000 cells were seeded in 100 µL of complete growth media per well in 96-well clear-bottom plates. After allowing cells to grow/adhere overnight, cells were treated with 100 µl per well of 2X drug solutions or vehicle in serum-free growth medium (8 doses ranging from either 40-1.25 µM or 20-0.625 µM in quadruplicate) and incubated for 72 h. Cell viability was assessed with alamarBlue reagent. Normalized fluorescence intensities were plotted with Prism and IC_{50} values were calculated from 4-parameter nonlinear regression curves. The reported IC_{50} values represent the average of at least three independent determinations (±SEM).

Flow cytometry analyses

To determine cell viability, HeLa or hTERT-RPE1 cells (250,000) were seeded onto 60 mm culture dishes. Subsequently, cells were treated with various concentrations of **Ir2** complex. After 3 days, cells were washed with PBS, detached using trypsin, resuspended in serum-free DMEM, counted and pelleted by centrifugation at 200 g. The pellets were then resuspended in PBS containing 1% BSA to

obtain at least 2 samples of 1 million cells/mL. One of the samples was treated with 7-AAD (7-Aminoactinomycin D) or DAPI at a concentration of 1 µg/ml, gently vortexed, and incubated on ice for 10 minutes before acquisition using a Gallios Flow Cytometer Analyzer (Beckman-Coulter). Mitochondrial membrane permeability was measured after staining with Mitotracker Red CMX-ROS according to manufacturer's instructions.

Real time cell analysis (RTCA)

xCELLigence E-plates were calibrated for a baseline definition and cells were seeded at 2000 cells per well in 100 µL complete medium. After about 24 h, drugs were added at the indicated concentration in triplicate and the cell index was measured over a period of 48-96 h (Real Time Cell Analyzer, Agilent).

Home-made "click-cocktail"

A stock solution (25x) containing 100 mM $CuSO_4$ and 500 mM THPTA was prepared in water and stored at 4°C. 200 mg/mL sodium ascorbate (10X) was prepared extemporaneously in buffer. The click-cocktail was prepared by diluting the alkynyl substrate at a concentration of 4.5 to 10 µM in the buffer, then adding the catalyst premixed solution and finally sodium ascorbate. The cocktail solution turns from blue to yellow, indicating the formation of the Cu(I) species.

Sample preparation for mass spectrometry chemoproteomics

About 30 million HEK293 cells were used per condition. Cells were cultured in 75 cm^2 flasks to reach 80 % confluency, washed with 10 mL of warm PBS prior to a 20 min treatment with **Ir2N$_3$** at 0.2 or 5 µM (in quintuplicate) in serum-free medium. Untreated cells were used as negative control. Cells were harvested in 10 mL of cold PBS and pelleted by centrifugation. Proteins were pulled down using the Click-&-Go™ protein enrichment kit (Click Chemistry Tools) to capture azide-modified proteins according to the manufacturer instructions with slight modifications. Lysis buffer was supplemented with protease and phosphatase inhibitor cocktail. After centrifugation, samples were then diafiltered at 4°C using 3 kDa cutoff VivaSpin®500 centrifuge filters (Sartorius) for 3 cycles of 20 min at 14,000

rpm, with addition of 125 µL of lysis buffer before each cycle. Beads suspended in 500 µL of digestion buffer (100 mM Tris-HCl pH 8.0, 2 mM CaCl2) were digested by 0.2 µg of trypsin/LysC for 1 h at 37 °C. Samples were loaded onto homemade SepPak C18 Tips packed by stacking three AttractSPE disk (#SPE-Disks-Bio-C18–100.47.20, Affinisep) into a 200 µL micropipette tip for desalting. Peptides were eluted with MeCN/H_2O 40:60 with 0.1 % formic acid and vacuum concentrated to dryness. The samples were resuspended in 10 µL of 0.3% TFA before LC-MS/MS analysis.

LC-MS/MS analysis

Samples (5 µL) were chromatographically separated on RSLCnano system (Ultimate 3000, Thermo Scientific) coupled online to an Orbitrap Eclipse mass spectrometer (Thermo Scientific). Peptides were first loaded onto a C18 trapped column (i.d. 75 µm x 2 cm, nanoViper Acclaim PepMapTM 100, Thermo Scientific) with eluent A (MeCN/H_2O 2:98 with 0.1 % formic acid) at a flow rate of 3.0 µL/min over 4 min and then switched for separation to a C18 column (i.d. 75 µm x 50 cm, nanoViper C18, 2 µm, 100 Å, Acclaim PepMapTM RSLC, Thermo Scientific) regulated to a temperature of 50°C with a linear gradient from 2 % to 25 % eluent B (MeCN with 0.1 % formic acid) at a flow rate of 300 nL/min over 91 min. MS1 data were collected in the Orbitrap (120,000 resolution; maximum injection time 60 ms; AGC 4e5). Charges states between 2 and 5 were required for MS2 analysis, and a 45 s dynamic exclusion window was used. MS2 scans were performed in the ion trap in rapid mode with HCD fragmentation (isolation window 1.2 Da; NCE 30 %; maximum injection time 60 ms; AGC $1e^4$). For identification, the data were searched against the Homo sapiens (UP000005640_9606) UniProt database using Sequest HT through Proteome Discoverer. Enzyme specificity was set to trypsin and a maximum of two miss cleavages sites were allowed. Oxidized methionine, Met-loss, Met-loss-Acetyl and N-terminal acetylation were set as variable modifications. Carbamidomethylation of cysteines was set as fixed modification. Maximum allowed mass deviation was set to 10 ppm for monoisotopic precursor ions and 0.6 Da for MS/MS peaks. The resulting files were further processed using myProMS. FDR calculation used Percolator and was set to 1% at the peptide level for the whole study.

Label-free quantification was performed by peptide Extracted Ion Chromatograms (XICs), reextracted across all conditions and computed with MassChroQ. For protein quantification, XICs from proteotypic peptides shared between compared conditions (TopN matching) and missed cleavages were allowed. Median and scale normalization was applied on the total signal to correct the XICs for each biological replicate (N=5 in each condition) for total signal and global variance biases. To estimate the significance of the change in protein abundance, a linear model (adjusted on peptides and biological replicates) was performed, and *p* values were adjusted using the Benjamini–Hochberg FDR procedure. Also, for each treatment condition (NT, 0.2 µM and 5 µM), the expression of proteins was computed as a molar proportion and mass percentage estimated by using top 359 (including proteins with less than 3 peptides) as the Protein Quantification Index and the direct proportionality model.[61] MS data are available via ProteomeXchange with identifier PXD038711.

DuoLink® PLA and immunofluorescence

100,000 hTERT-RPE1 cells were seeded on 12 mm diameter coverslips and cultured overnight in complete medium. Cells were washed with PBS and incubated for 15 min in serum-free medium containing 0, 0.2 or 5 µM **Ir2N$_3$**. Cells were washed and fixed for 15 min at room temperature in 4 % PFA in PBS containing 1 µg/mL of Hoechst 33342. After four PBS washes, the click reaction was performed with the home-made click cocktail containing 5 µM biotin PEG4-alkyne for 30 min at room temperature. Cells were washed twice with PBS and incubated for 90 min with 3 % BSA in PBS-0.3 % Triton X-100. Coverslips were incubated overnight at 4°C with Mouse anti-Biotin antibody (1:1000) and/or Rabbit anti-[FLNB, HSP90, GRP78, P34-Arc/ARPC2] (1:100). The DuoLink® proximity ligation assay was carried out according to the supplier's instructions and all slides were incubated for 1 h with an Alexa488-anti-Rabbit secondary antibody (or Alexa488-anti-mouse for a subset of controls). Slides were imaged using a Leica DM4 B upright microscope with a 63x objective and signal intensities were quantified using Fiji.

Effect of Ir2 on the activities of HSP molecular chaperones *in vitro*

Purified recombinant Heat Shock Proteins (cloning and purification reported in SI) were diluted in labeling buffer (25 mM Tris-HCl pH7.5; 150 mM NaCl; 5% glycerol) to a final concentration of 50 µM. **Ir2** was added to final concentrations of 0, 5, 50 or 500 µM and 5 % DMSO. Samples were incubated at room temperature during one hour and labeled proteins were separated from **Ir2** and DMSO by 5 cycles of diafiltration (12,000 g, 4°C, molecular cutoff 10 kDa, Sartorius) adding 5 volumes of labeling buffer before each cycle. **Ir2** was undetectable in the 5 and 50 µM samples but still present at 8 µM in the 500 µM sample. Proteins were further purified by size-exclusion chromatography with PD-10 column (Cytiva) using labeling buffer as eluent to eliminate remaining free **Ir2**. Samples were concentrated and the protein concentration measured by BCA assay kit. Steady-state ATPase activity of Heat Shock Proteins was evaluated by a coupled enzymatic assay (PK/LDH) monitoring the oxidation of NADH as described previously[62] with a modified reaction buffer (50 mM HEPES pH 7.5, 100 mM KCl, 5 mM ATP, 5 mM $MgCl_2$) in 96-well plates on a CLARIOstar reader (BMG Labtech). Heat Shock Protein concentrations were either 10 µM for HSP90 or 5 µM for HSP70. The HSP90 ATPase activity was corrected by subtraction of the background ATPase activity after addition of 50 µM radicicol. QuantiLum Recombinant Luciferase was diluted to 55 µM in denaturation buffer containing 6 M Guanidium/HCl and 1 mM DTT during 30 min at room temperature. Denatured luciferase was diluted 125 times (0.4 µM) in renaturation buffer (20 mM Tris-HCl pH 7.5, 50 mM KCl, 5 mM $MgCl_2$, 1 mM DTT) supplemented with HSP samples treated with **Ir2** or DMSO. Final concentrations of recombinant chaperones and cochaperones were: 10 µM HSP70, 2 µM DNAJB1 and, for the evaluation of HSP90 activity, 0.5 µM STIP1 and 2 µM HSP90. Refolded luciferase activity was measured by mixing of 5 µL aliquots of labeled samples with 120 µL of luciferase buffer (20 mM Tris-HCl pH=7.5; 200 µM luciferin; 0.5 mM ATP; 10 mM $MgCl_2$). The chemiluminescence was measured on a CLARIOStar plate reader (BMG Labtech). The percentage of refolded luciferase was evaluated relatively to the activity of native luciferase.

Sample preparation for fluorescence imaging

50,000 HuH-7 cells were seeded on 14 mm coverslips (#1.5) in a 12-well plate and cultured in complete medium. The next day, cells were washed and treated for 1 h with **Ir2N$_3$** at 1 or 5 µM in serum-free media. Cells were fixed with 4 % PFA in PBS and washed three times with PBS. Specimens were blocked and permeabilized using PBS containing 3 % BSA and 0.5 % Triton X-100 during 30 min at room temperature. Coverslips were washed with PBS and incubated with the home-made click cocktail containing 4.5 µM FAM alkyne during 30 min. Finally, samples were washed three times with PBS and stained with 1 µg/mL Hoechst 33342 and AlexaFluor 633-Phalloidin in PBS during 30 min. Coverslips were washed with PBS and mounted in Prolong Diamond mounting medium.

Super resolution fluorescence microscopy

Acquisitions were performed on an inverted AXIO OBSERVER 7 LSM 980 6 CH AIRYSCAN 2 (Zeiss), with a 63x oil immersion NA 1.4 objective, the following excitation laser lines: 405 nm, 488 nm, 639 nm and the corresponding bandpass filters: BP 422-477, BP 495-550 and BP 655-720. Images were taken and processed with the Airyscan 2 technology in SR (Super-Resolution) mode.

Micropatterning

35-mm dishes with a #1.5H glass coverslip bottom imprinted with 50 µm cell location grid (IBIDI) were used as patterning substrates. Glass bottoms were first glowed with a plasma cleaner to ensure hydrophilicity, then coated for 30 min at room temperature with 0.1 mg/mL PLL. After 3 washes with PBS, the dishes were incubated with a freshly made solution of 100 mg/mL PEG-SVA in HEPES buffer pH 8-8.5 for 45 min at room temperature. Photopatterning: Substrates were thoroughly washed with deionized water and patterns were imprinted using a gel photo-initiator (PLPP, Alvéole) and a photomicropatterning device (PRIMO, Alvéole) equipped with a UV laser, delivering doses of 15 mJ/mm^2. The shapes of the patterns (crossbows 40 x 40 µm^2, discs of 35 or 42 µm diameter, arrowheads 40 x 30 µm^2) were imprinted using an inverted Axio Observer 7 (Zeiss) with a 20x objective, their position and repetition on the substrate surface were managed using the associated plug-in (Leonardo, Alvéole).

Sample preparation for correlative light and scanning electron microscopy (CLSEM)

Buffers used were PEM (100 mM PIPES, 1 mM $MgCl_2$, 1 mM EGTA) and Extraction Buffer[44] (PEM, 1% Triton X-100, 1% Phalloidin-Alexa350). Micropatterned IBIDI meshed dishes were coated with 50 µg/mL fibronectin in PBS for 30 min at 37°C and washed with PBS. Dishes were seeded with 100,000 hTERT-RPE1 cells in 3 mL complete medium, left to adhere for 2 h. Cells were treated for 15 min in serum-free medium with either 5 µM, 10 µM **Ir2N$_3$** or vehicle. Dishes were washed with 3 mL of warm HBSS (with Ca^{2+} and Mg^{2+}) and extracted with 200 µL of extraction buffer during 5 min, then cells were fixed with 2 % glutaraldehyde (GA) in PBS for 20 min at room temperature. Cells were washed 5 times with PBS and samples were incubated for 30 min at room temperature with the click cocktail containing 4.5 µM FAM alkyne to label **Ir2N$_3$**. Cells were washed 3 times with PBS, and GA was quenched with two 4 min baths of 1% $NaBH_4$ in PBS followed by 3 PBS washes. Samples were kept at 4°C overnight in PBS. Actin cytoskeleton was re-stained for 30 min with Phalloidin-Alexa350 followed by 3 PBS washes. Cell nuclei were stained using DRAQ5 for 20 min followed by 3 PBS washes. After light microscopy acquisitions, samples were sequentially post-fixed for 10 min each with 1 % aqueous tannic acid then 1 % aqueous uranyl acetate before extensive washing in distilled water,[63] before gradual dehydration with ethanol and hexamethyldisilazane, then drying under vacuum. Finally, micropatterned slides were removed from the dishes, mounted on stubs, and coated by sputtering of 2-3 nm of chromium (ACE600, Leica microsystems).

Scanning electron microscopy

Field-Emission scanning electron microscopy was operated at 1.5 kV (GeminiSEM500, Zeiss) with a 15 µm objective aperture diameter (19 pA). Secondary electrons were collected with an in-lens detector and high-sensitivity Everhart-Thornley (SE2) detectors, scan speed and line integration were adjusted during observation and images were averaged from both detectors. Directionality analysis: A set of 6.25 x 6.25 μm^2 square images were acquired in the cortical region of 7-8 cells per condition at high magnification. The images were filtered with a bandpass FFT filter, and the local gradient

orientation was analyzed (Directionality Plugin, Fiji) over 36 directions from 0° (east direction) to 180° (counterclockwise), giving a Gaussian distribution around the main direction of filaments. The resulting HWHM (half-width at half-maximum) of fitted curves was calculated using Prism.

Sample preparation for correlative Light-XRF analysis

Silicon nitride membranes (Silson Ltd) consisting in square silicon frames of 5 x 5 mm^2 and 200 µm thickness with a central Si_3N_4 membrane of 1.5 x 1.5 mm^2 and 500 nm thickness were used for cell culture and allow contaminant-free XRF low background signal. During manufacturing, a second, smaller (0.1 x 0.1 mm^2) membrane is added in one of the corners of the silicon frame to serve as orientation object. Membranes were coated for 15 min with 50 µg/mL fibronectin in PBS at room temperature, thoroughly washed with PBS and seeded with 4000 – 8000 hTERT-RPE1 cells in 10 µL of complete medium. Cells were incubated for 3-4 h at 37°C and 5% CO_2 to adhere and spread on the substrates. They were stained for 90 min with SPY650-FastAct, including 30 min of co-staining with 100 nM Mitotracker Green FM and 5 µg/mL Hoechst 33342. Membranes were washed and further incubated in medium containing 5% FBS ± 5 µM **Ir2** for 15 min, then rinsed with PBS and serum-free medium. Samples were quickly rinsed with 150 mM ammonium acetate solution followed by manual blotting and plunge-freezing into liquid ethane chilled with liquid nitrogen.[64]

Cryo-fluorescence light microscopy (cryo-FLM)

Plunge-frozen cells were imaged using cryo-CLEM Thunder system (Leica) equipped with a ceramic-tipped, 0.9 NA, 50X lens. The brightfield and band pass filter cubes of GFP, DAPI, and Y5 were used. A complete mosaic of the 1.5 x 1.5 mm Si_3N_4 active area containing vitrified cellular region of interest was registered with the collection for each field of view of a Z-stack projection over ~ 20 µm. Images acquired at 88 K Large Volume Computational Clearance (LVCC) from Leica LAS X Thunder package were applied for fluorescence image deconvolution and blurring reduction on the cryo-FLM image stacks.

SR-XRF microscopy

The ID16A end station is under high-vacuum and is equipped with a cryostage to allow measurements of frozen-hydrated sample kept at 120K and the combined used of LEICA EM-VCM, EM-VCT systems allows the cryotransfer. Nano-positioning is performed by a piezo-driven short-range hexapod stage regulated with the metrology of twelve capacitive sensors. All scanning uses "on-the-fly" acquisition with the sample translated at constant speed in the horizontal direction.[65] The beam was focused to 26 × 42 nm^2 (vertical × horizontal) using a pair of Kirkpatrick-Baez mirrors.[66] The fluorescence signal emitted from each sample pixel was recorded by two custom multi-element Silicon Drift Detectors (SDD) placed on both sides of the sample and facing each other at 90° from the incident x-ray beam. A multi-element SDD (Hitachi Ltd.) and an ARDESIA-16 spectrometer based on monolithic SDD array[67] were used. The resulting XRF spectra were fitted pixel by pixel using a dedicated Python script to correct for detector deadtime and perform normalization for variation of the incident X-ray beam. The elemental areal mass concentration was calculated using the Fundamental Parameters (FP) approach implemented in PyMca software package and a reference standard material containing element of certified concentration (RF7-200-S2371 from AXO, Dresden, Germany) with uniform mass depositions in the range of ng/mm^2 (1-3 atomic layers). The resulting elemental areal mass density maps were visualized with ImageJ software.

Statistics

Statistical significance of the reported data was systematically calculated as described in the figure legends.

Ancillary information

Supporting information

Resources tables, Heat Shock Proteins cloning and purification protocol, supplementary figures S1-S9, crystal data and structure refinement, NMR spectra, HPLC traces (PDF); Proteomic data including Protein lists and GO analyses (XLSX); Molecular Formula Strings (CSV); Videos illustrating cell motility and actin cytoskeleton dynamics (AVI).

Corresponding authors information

Correspondence: michele.salmain@sorbonne-universite.fr or joelle.sobczak@inserm.fr

Abbreviations Used

BODIPY, boron dipyrromethene; CCCP, carbonyl cyanide m-chlorophenyl hydrazone; CLSEM, correlative light and scanning electron microscopy; ct-DNA, calf thymus DNA; CuAAC, copper-catalyzed azide-alkyne cycloaddition; DAPI, 4',6-diamidino-2-phenylindole; DNAJB1, DnaJ, homolog subfamily B member 1; FAM, fluorescein; GO, gene ontology, GSH, glutathione; H2AX, H2A histone family member X; HO, Hoechst 33342; HWHM, half-width at half-maximum; ICP-OES, inductively coupled plasma – optical emission spectroscopy; LM, light microscopy; MTR, Mitotracker Red™; Nrf2, nuclear factor erythroid 2-related factor; PLA, protein ligation assay; PLL, Poly-L-lysine; RTCA, real time cell analysis; SD, standard deviation; SEM, standard error of measurement; STIP1, stress induced phosphoprotein 1; THPTA, tris(benzyltriazolylmethyl)amine; XRF, X-ray fluorescence.

Acknowledgements

We thank Dr. Patricia Forgez for the gift of ovarian cell lines, Chelly Accipe and Lucile Diot for technical support. We are indebted to Annie Munier, Romain Morichon (CISA platform), Benoit Caron (ALIPP6 platform) and Cédric Przybylski (MSU^3 platform). We are grateful for the help of Louise Bonnemay, Matthieu Opitz and Hélène Delobel from Alvéole company and Fabrice Schmitt

from Zeiss company to imprint micropatterned substrates. PM thanks L. Qin, J. Henri and F. Georgescauld for their help in expression vector design and initial set-up of functional assays.

This work was supported by a Ph.D. fellowship from Sorbonne Université and post-doctoral fellowships from the PCSI program of ITMO Cancer (20CP175-00; R. Ramos and S. Amhaz), SiRIC CURAMUS financially supported by the French National Cancer Institute, the French Ministry of Solidarity and Health and Inserm (R20113DD; J.S-T), INCa-DGOS-Inserm_12560 (J.S-T), PCSI program of ITMO Cancer supported by Inserm and Aviesan (grant no. 20CP175-00; M.S and J.S-T). We acknowledge the European Synchrotron Research Facility (ESRF) for granting beamtime through experiment LS-3136 at beamline ID16A. P.M. acknowledges the financial support of the French National Research Agency as part of the "Investissements d'Avenir" Program (LabEx Dynamo ANR-11-LABX-0011-01) and ANR16-CE11-0032-03, the French Plan Cancer and the Fondation ARC (PDF20151203636). MS analysis was performed with financial support from "la Région Ile-de-France" (N°EX061034) and ITMO Cancer of Aviesan and INCa on funds administered by Inserm (N°21CQ016-00). The funders had no role in study design, data collection and analysis, decision to publish or preparation of the manuscript.

Author contributions

RR Investigation, formal analysis, visualization, writing of original draft. SA Investigation, formal analysis, visualization. AK, CB, Conceptualization, writing review and editing. MT FL JF SB PM TC CBe DL FD SA Data acquisition, formal analysis. AC CC mass spectrometry data acquisition. MS, JST* Funding acquisition, data curation, project administration, manuscript editing, joint supervision. All authors analyzed data and discussed results. The manuscript was written and edited through contributions from all the authors.

Declaration of interests

The authors declare no competing interests.

References

(1) Sharma, A. S.; Sudhindra, P.; Roy, N.; Paira, P. Advances in Novel Iridium (III) Based Complexes for Anticancer Applications: A Review. *Inorganica Chim. Acta* **2020**, *513*, 119925. https://doi.org/10.1016/j.ica.2020.119925.

(2) Ho, P.-Y.; Ho, C.-L.; Wong, W.-Y. Recent Advances of Iridium(III) Metallophosphors for Health-Related Applications. *Coord. Chem. Rev.* **2020**, *413*, 213267. https://doi.org/10.1016/j.ccr.2020.213267.

(3) Huang, H.; Banerjee, S.; Qiu, K.; Zhang, P.; Blacque, O.; Malcomson, T.; Paterson, M. J.; Clarkson, G. J.; Staniforth, M.; Stavros, V. G.; Gasser, G.; Chao, H.; Sadler, P. J. Targeted Photoredox Catalysis in Cancer Cells. *Nat. Chem.* **2019**, *11* (11), 1041–1048. https://doi.org/10.1038/s41557-019-0328-4.

(4) Caporale, C.; Massi, M. Cyclometalated Iridium(III) Complexes for Life Science. *Coord. Chem. Rev.* **2018**, *363*, 71–91. https://doi.org/10.1016/j.ccr.2018.02.006.

(5) Lord, R. M.; McGowan, P. C. Organometallic Iridium Arene Compounds: The Effects of C-Donor Ligands on Anticancer Activity. *Chem. Lett.* **2019**, *48* (8), 916–924. https://doi.org/10.1246/cl.190179.

(6) Acuna, M.; Rubio, A.; Martinez-Alonso, M.; Busto, N.; Rodriguez, A.; Davila-Ferreira, N.; Smythe, C.; Espino, G.; Garcia, B.; Dominguez, F. Targets, Mechanisms and Cytotoxicity of Half-Sandwich Ir(III) Complexes Are Modulated by Structural Modifications on the Benzazole Ancillary Ligand. *Cancers* **2023**, *15* (1). https://doi.org/10.3390/cancers15010107.

(7) Wang, M.; Li, H.; Deng, D.; Su, Y.; Su, Z. Performance of Ir(III)-Based Anticancer Agents in the Treatment of Cisplatin-Resistant Cancer Cells. *ChemMedChem* **2022**, *17* (16). https://doi.org/10.1002/cmdc.202200273.

(8) Roy, N.; Sen, U.; Ray Chaudhuri, S.; Muthukumar, V.; Moharana, P.; Paira, P.; Bose, B.; Gauthaman, A.; Moorthy, A. Mitochondria Specific Highly Cytoselective Iridium(III)–Cp*

Dipyridophenazine (Dppz) Complexes as Cancer Cell Imaging Agents. *Dalton Trans.* **2021**, *50* (6), 2268–2283. https://doi.org/10.1039/D0DT03586F.

(9) De Palo, A.; Draca, D.; Murrali, M. G.; Zacchini, S.; Pampaloni, G.; Mijatovic, S.; Maksimovic-Ivanic, D.; Marchetti, F. A Comparative Analysis of the In Vitro Anticancer Activity of Iridium(III) {η5-C5Me4R} Complexes with Variable R Groups. *Int. J. Mol. Sci.* **2021**, *22* (14), 7422. https://doi.org/10.3390/ijms22147422.

(10) Liu, Z.; Salassa, L.; Habtemariam, A.; Pizarro, A. M.; Clarkson, G. J.; Sadler, P. J. Contrasting Reactivity and Cancer Cell Cytotoxicity of Isoelectronic Organometallic Iridium(III) Complexes. *Inorg. Chem.* **2011**, *50* (12), 5777–5783. https://doi.org/10.1021/ic200607j.

(11) Ritacco, I.; Russo, N.; Sicilia, E. DFT Investigation of the Mechanism of Action of Organoiridium(III) Complexes As Anticancer Agents. *Inorg. Chem.* **2015**, *54* (22), 10801–10810. https://doi.org/10.1021/acs.inorgchem.5b01832.

(12) Liu, Z.; Romero-Canelón, I.; Qamar, B.; Hearn, J. M.; Habtemariam, A.; Barry, N. P. E.; Pizarro, A. M.; Clarkson, G. J.; Sadler, P. J. The Potent Oxidant Anticancer Activity of Organoiridium Catalysts. *Angew. Chem. Int. Ed.* **2014**, *53* (15), 3941–3946. https://doi.org/10.1002/anie.201311161.

(13) Ramos, R.; Zimbron, J. M.; Thorimbert, S.; Chamoreau, L.-M.; Munier, A.; Botuha, C.; Karaiskou, A.; Salmain, M.; Sobczak-Thépot, J. Insights into the Antiproliferative Mechanism of (C^N)-Chelated Half-Sandwich Iridium Complexes. *Dalton Trans.* **2020**, *49* (48), 17635–17641. https://doi.org/10.1039/D0DT03414B.

(14) Liu, Z.; Sadler, P. J. Formation of Glutathione Sulfenate and Sulfinate Complexes by an Organoiridium(III) Anticancer Complex. *Inorg Chem Front* **2014**, *1* (9), 668–672. https://doi.org/10.1039/C4QI00098F.

(15) Qi, Y.; Liu, Z.; Li, H.; Sadler, P. J.; O'Connor, P. B. Mapping the Protein-Binding Sites for Novel Iridium(III) Anticancer Complexes Using Electron Capture Dissociation: Protein-Binding

Sites for Ir-Based Anticancer Complexes. *Rapid Commun. Mass Spectrom.* **2013**, *27* (17), 2028–2032. https://doi.org/10.1002/rcm.6643.

(16) Carrasco, A. C.; Rodríguez-Fanjul, V.; Habtemariam, A.; Pizarro, A. M. Structurally Strained Half-Sandwich Iridium(III) Complexes As Highly Potent Anticancer Agents. *J. Med. Chem.* **2020**, *63* (8), 4005–4021. https://doi.org/10.1021/acs.jmedchem.9b02000.

(17) Ramos, R.; Gilles, J.-F.; Morichon, R.; Przybylski, C.; Caron, B.; Botuha, C.; Karaiskou, A.; Salmain, M.; Sobczak-Thépot, J. Cytotoxic BODIPY-Appended Half-Sandwich Iridium(III) Complex Forms Protein Adducts and Induces ER Stress. *J. Med. Chem.* **2021**, *64* (22), 16675–16686. https://doi.org/10.1021/acs.jmedchem.1c01335.

(18) Steel, T. R.; Hartinger, C. G. Metalloproteomics for Molecular Target Identification of Protein-Binding Anticancer Metallodrugs. *Metallomics* **2020**, *12* (11), 1627–1636. https://doi.org/10.1039/d0mt00196a.

(19) Wang, H.; Zhou, Y.; Xu, X.; Li, H.; Sun, H. Metalloproteomics in Conjunction with Other Omics for Uncovering the Mechanism of Action of Metallodrugs: Mechanism-Driven New Therapy Development. *Curr. Opin. Chem. Biol.* **2020**, *55*, 171–179. https://doi.org/10.1016/j.cbpa.2020.02.006.

(20) Xiong, X.; Liu, L.-Y.; Mao, Z.-W.; Zou, T. Approaches towards Understanding the Mechanism-of-Action of Metallodrugs. *Coord. Chem. Rev.* **2022**, *453*, 214311. https://doi.org/10.1016/j.ccr.2021.214311.

(21) Meier, S. M.; Kreutz, D.; Winter, L.; Klose, M. H. M.; Cseh, K.; Weiss, T.; Bileck, A.; Alte, B.; Mader, J. C.; Jana, S.; Chatterjee, A.; Bhattacharyya, A.; Hejl, M.; Jakupec, M. A.; Heffeter, P.; Berger, W.; Hartinger, C. G.; Keppler, B. K.; Wiche, G.; Gerner, C. An Organoruthenium Anticancer Agent Shows Unexpected Target Selectivity For Plectin. *Angew. Chem. Int. Ed.* **2017**, *56* (28), 8267–8271. https://doi.org/10.1002/anie.201702242.

(22) Yin, H.; Gao, J.; Chen, X.; Ma, B.; Yang, Z.; Tang, J.; Wang, B.; Chen, T.; Wang, C.;

Gao, S.; Zhang, J. A Gallium(III) Complex That Engages Protein Disulfide Isomerase A3 (PDIA3) as an Anticancer Target. *Angew. Chem. Int. Ed.* **2020**, *59* (45), 20147–20153. https://doi.org/10.1002/anie.202008432.

(23) Neuditschko, B.; Legin, A. A.; Baier, D.; Schintlmeister, A.; Reipert, S.; Wagner, M.; Keppler, B. K.; Berger, W.; Meier-Menches, S. M.; Gerner, C. Interaction with Ribosomal Proteins Accompanies Stress Induction of the Anticancer Metallodrug BOLD-100/KP1339 in the Endoplasmic Reticulum. *Angew. Chem. Int. Ed.* **2021**, *60* (10), 5063–5068. https://doi.org/10.1002/anie.202015962.

(24) Neuditschko, B.; King, A. P.; Huang, Z.; Janker, L.; Bileck, A.; Borutzki, Y.; Marker, S. C.; Gerner, C.; Wilson, J. J.; Meier-Menches, S. M. An Anticancer Rhenium Tricarbonyl Targets Fe−S Cluster Biogenesis in Ovarian Cancer Cells. *Angew. Chem. Int. Ed.* **2022**, *61* (43), e202209136. https://doi.org/10.1002/anie.202209136.

(25) Babak, M. V.; Meier, S. M.; Huber, K. V. M.; Reynisson, J.; Legin, A. A.; Jakupec, M. A.; Roller, A.; Stukalov, A.; Gridling, M.; Bennett, K. L.; Colinge, J.; Berger, W.; Dyson, P. J.; Superti-Furga, G.; Keppler, B. K.; Hartinger, C. G. Target Profiling of an Antimetastatic RAPTA Agent by Chemical Proteomics: Relevance to the Mode of Action. *Chem. Sci.* **2015**, *6* (4), 2449–2456. https://doi.org/10.1039/C4SC03905J.

(26) Ming, X.; Groehler, A.; Michaelson-Richie, E. D.; Villalta, P. W.; Campbell, C.; Tretyakova, N. Y. Mass Spectrometry Based Proteomics Study of Cisplatin-Induced DNA–Protein Cross-Linking in Human Fibrosarcoma (HT1080) Cells. *Chem. Res. Toxicol.* **2017**, *30* (4), 980–995. https://doi.org/10.1021/acs.chemrestox.6b00389.

(27) Hu, D.; Liu, Y.; Lai, Y.-T.; Tong, K.-C.; Fung, Y.-M.; Lok, C.-N.; Che, C.-M. Anticancer Gold(III) Porphyrins Target Mitochondrial Chaperone Hsp60. *Angew. Chem. Int. Ed.* **2016**, *55* (4), 1387–1391. https://doi.org/10.1002/anie.201509612.

(28) Fung, S. K.; Zou, T.; Cao, B.; Lee, P.-Y.; Fung, Y. M. E.; Hu, D.; Lok, C.-N.; Che, C.-M. Cyclometalated Gold(III) Complexes Containing N-Heterocyclic Carbene Ligands Engage

Multiple Anti-Cancer Molecular Targets. *Angew. Chem. Int. Ed.* **2017**, *56* (14), 3892–3896. https://doi.org/10.1002/anie.201612583.

(29) Xiong, X.; Huang, K.-B.; Wang, Y.; Cao, B.; Luo, Y.; Chen, H.; Yang, Y.; Long, Y.; Liu, M.; Chan, A. S. C.; Liang, H.; Zou, T. Target Profiling of an Iridium(III)-Based Immunogenic Cell Death Inducer Unveils the Engagement of Unfolded Protein Response Regulator BiP. *J. Am. Chem. Soc.* **2022**, *144* (23), 10407–10416. https://doi.org/10.1021/jacs.2c02435.

(30) Yan, X.; Li, J.; Liu, Q.; Peng, H.; Popowich, A.; Wang, Z.; Li, X.-F.; Le, X. C. *P* -Azidophenylarsenoxide: An Arsenical "Bait" for the In Situ Capture and Identification of Cellular Arsenic-Binding Proteins. *Angew. Chem. Int. Ed.* **2016**, *55* (45), 14051–14056. https://doi.org/10.1002/anie.201608006.

(31) Hu, X.; Li, H.; Ip, T. K.-Y.; Cheung, Y. F.; Koohi-Moghadam, M.; Wang, H.; Yang, X.; Tritton, D. N.; Wang, Y.; Wang, Y.; Wang, R.; Ng, K.-M.; Naranmandura, H.; Tse, E. W.-C.; Sun, H. Arsenic Trioxide Targets Hsp60, Triggering Degradation of P53 and Survivin. *Chem. Sci.* **2021**, *12* (32), 10893–10900. https://doi.org/10.1039/D1SC03119H.

(32) Cunningham, R. M.; DeRose, V. J. Platinum Binds Proteins in the Endoplasmic Reticulum of *S. Cerevisiae* and Induces Endoplasmic Reticulum Stress. *ACS Chem. Biol.* **2017**, *12* (11), 2737–2745. https://doi.org/10.1021/acschembio.7b00553.

(33) OCDE. *Test No. 117: Partition Coefficient (n-Octanol/Water), HPLC Method*; 2022. https://doi.org/10.1787/9789264069824-en.

(34) Hearn, J. M.; Hughes, G. M.; Romero-Canelón, I.; Munro, A. F.; Rubio-Ruiz, B.; Liu, Z.; Carragher, N. O.; Sadler, P. J. Pharmaco-Genomic Investigations of Organo-Iridium Anticancer Complexes Reveal Novel Mechanism of Action. *Metallomics* **2018**, *10* (1), 93–107. https://doi.org/10.1039/C7MT00242D.

(35) Bilan, D. S.; Belousov, V. V. HyPer Family Probes: State of the Art. *Antioxid. Redox Signal.* **2016**, *24* (13), 731–751. https://doi.org/10.1089/ars.2015.6586.

(36) Ma, Q. Role of Nrf2 in Oxidative Stress and Toxicity. *Annu. Rev. Pharmacol. Toxicol.* **2013**, *53* (1), 401–426. https://doi.org/10.1146/annurev-pharmtox-011112-140320.

(37) Jin, P.; Jiang, J.; Zhou, L.; Huang, Z.; Nice, E. C.; Huang, C.; Fu, L. Mitochondrial Adaptation in Cancer Drug Resistance: Prevalence, Mechanisms, and Management. *J. Hematol. Oncol.* **2022**, *15* (1), 97. https://doi.org/10.1186/s13045-022-01313-4.

(38) Srinivas, U. S.; Tan, B. W. Q.; Vellayappan, B. A.; Jeyasekharan, A. D. ROS and the DNA Damage Response in Cancer. *Redox Biol.* **2019**, *25*, 101084. https://doi.org/10.1016/j.redox.2018.101084.

(39) Perrin, L.; Carmona, A.; Roudeau, S.; Ortega, R. Evaluation of Sample Preparation Methods for Single Cell Quantitative Elemental Imaging Using Proton or Synchrotron Radiation Focused Beams. *J. Anal. At. Spectrom.* **2015**, *30* (12), 2525–2532. https://doi.org/10.1039/C5JA00303B.

(40) Carmona, A.; Devès, G.; Roudeau, S.; Cloetens, P.; Bohic, S.; Ortega, R. Manganese Accumulates within Golgi Apparatus in Dopaminergic Cells as Revealed by Synchrotron X-Ray Fluorescence Nanoimaging. *ACS Chem. Neurosci.* **2010**, *1* (3), 194–203. https://doi.org/10.1021/cn900021z.

(41) Das, S.; Carmona, A.; Khatua, K.; Porcaro, F.; Somogyi, A.; Ortega, R.; Datta, A. Manganese Mapping Using a Fluorescent Mn2+ Sensor and Nanosynchrotron X-Ray Fluorescence Reveals the Role of the Golgi Apparatus as a Manganese Storage Site. *Inorg. Chem.* **2019**, *58* (20), 13724–13732. https://doi.org/10.1021/acs.inorgchem.9b01389.

(42) Bertrand, B.; Sobczak-Thépot, J.; Salmain, M.; Ramos, R. Elemental Mapping of Gold- and Iridium-Based Anticancer Drug Candidates in Single Mammalian Cells, 2022. https://doi.org/10.15151/ESRF-ES-946451005.

(43) Cañeque, T.; Müller, S.; Rodriguez, R. Visualizing Biologically Active Small Molecules in Cells Using Click Chemistry. *Nat. Rev. Chem.* **2018**, *2* (9), 202–215.

https://doi.org/10.1038/s41570-018-0030-x.

(44) Svitkina, T. M. Actin Cell Cortex: Structure and Molecular Organization. *Trends Cell Biol.* **2020**, *30* (7), 556–565. https://doi.org/10.1016/j.tcb.2020.03.005.

(45) Théry, M. Micropatterning as a Tool to Decipher Cell Morphogenesis and Functions. *J. Cell Sci.* **2010**, *123* (24), 4201–4213. https://doi.org/10.1242/jcs.075150.

(46) Sibert, B. S.; Kim, J. Y.; Yang, J. E.; Wright, E. R. Micropatterning Transmission Electron Microscopy Grids to Direct Cell Positioning within Whole-Cell Cryo-Electron Tomography Workflows. *J. Vis. Exp.* **2021**, No. 175, 62992. https://doi.org/10.3791/62992.

(47) Liu, Z.; Habtemariam, A.; Pizarro, A. M.; Fletcher, S. A.; Kisova, A.; Vrana, O.; Salassa, L.; Bruijnincx, P. C. A.; Clarkson, G. J.; Brabec, V.; Sadler, P. J. Organometallic Half-Sandwich Iridium Anticancer Complexes. *J. Med. Chem.* **2011**, *54* (8), 3011–3026. https://doi.org/10.1021/jm2000932.

(48) Xu, Z.; Zhang, Y.; Zhang, S.; Jia, X.; Zhong, G.; Yang, Y.; Du, Q.; Li, J.; Liu, Z. Novel Half-Sandwich Iridium O^C (Carbene)-Complexes: In Vitro and in Vivo Tumor Growth Suppression and pro-Apoptosis via ROS-Mediated Cross-Talk between Mitochondria and Lysosomes. *Cancer Lett.* **2019**, *447*, 75–85. https://doi.org/10.1016/j.canlet.2019.01.018.

(49) Shao, M.; Yao, M.; Liu, X.; Gao, C.; Liu, W.; Guo, J.; Zong, J.; Sun, X.; Liu, Z. In Vitro and In Vivo of Triphenylamine-Appended Fluorescent Half-Sandwich Iridium(III) Thiosemicarbazones Antitumor Complexes. *Inorg. Chem.* **2021**, *60* (22), 17063–17073. https://doi.org/10.1021/acs.inorgchem.1c02250.

(50) Zhao, X.; Zhang, J.; Zhang, W.; Guo, Z.; Wei, W.; Wang, X.; Zhao, J. A Chiral Fluorescent Ir(Iii) Complex That Targets the GPX4 and ErbB Pathways to Induce Cellular Ferroptosis. *Chem Sci* **2023**, *14* (5), 1114–1122. https://doi.org/10.1039/d2sc06171f.

(51) Hearn, J. M.; Romero-Canelón, I.; Qamar, B.; Liu, Z.; Hands-Portman, I.; Sadler, P. J. Organometallic Iridium(III) Anticancer Complexes with New Mechanisms of Action: NCI-60

Screening, Mitochondrial Targeting, and Apoptosis. *ACS Chem. Biol.* **2013**, *8* (6), 1335–1343. https://doi.org/10.1021/cb400070a.

(52) Zhang, W.-Y.; Banerjee, S.; Hughes, G. M.; Bridgewater, H. E.; Song, J.-I.; Breeze, B. G.; Clarkson, G. J.; Coverdale, J. P. C.; Sanchez-Cano, C.; Ponte, F.; Sicilia, E.; Sadler, P. J. Ligand-Centred Redox Activation of Inert Organoiridium Anticancer Catalysts. *Chem. Sci.* **2020**, *11* (21), 5466–5480. https://doi.org/10.1039/D0SC00897D.

(53) Murillo, M. I.; Gaiddon, C.; Le Lagadec, R. Targeting of the Intracellular Redox Balance by Metal Complexes towards Anticancer Therapy. *Front. Chem.* **2022**, *10*, 967337. https://doi.org/10.3389/fchem.2022.967337.

(54) Liu, Z.; Habtemariam, A.; Pizarro, A. M.; Clarkson, G. J.; Sadler, P. J. Organometallic Iridium(III) Cyclopentadienyl Anticancer Complexes Containing C,N-Chelating Ligands. *Organometallics* **2011**, *30* (17), 4702–4710. https://doi.org/10.1021/om2005468.

(55) Tong, K. K. H.; Hanif, M.; Movassaghi, S.; Sullivan, M. P.; Lovett, J. H.; Hummitzsch, K.; Söhnel, T.; Jamieson, S. M. F.; Bhargava, S. K.; Harris, H. H.; Hartinger, C. G. Triazolyl-Functionalized *N* -Heterocyclic Carbene Half-Sandwich Compounds: Coordination Mode, Reactivity and *in Vitro* Anticancer Activity. *ChemMedChem* **2021**, *16* (19), 3017–3026. https://doi.org/10.1002/cmdc.202100311.

(56) Conesa, J. J.; Carrasco, A. C.; Rodríguez-Fanjul, V.; Yang, Y.; Carrascosa, J. L.; Cloetens, P.; Pereiro, E.; Pizarro, A. M. Unambiguous Intracellular Localization and Quantification of a Potent Iridium Anticancer Compound by Correlative 3D Cryo X-Ray Imaging. *Angew. Chem. Int. Ed.* **2020**, *59* (3), 1270–1278. https://doi.org/10.1002/anie.201911510.

(57) Taddei, M.; Giannoni, E.; Fiaschi, T.; Chiarugi, P. Anoikis: An Emerging Hallmark in Health and Diseases. *J. Pathol.* **2012**, *226* (2), 380–393. https://doi.org/10.1002/path.3000.

(58) Imstepf, S.; Pierroz, V.; Rubbiani, R.; Felber, M.; Fox, T.; Gasser, G.; Alberto, R. Organometallic Rhenium Complexes Divert Doxorubicin to the Mitochondria. *Angew. Chem. Int. Ed.*

2016, *55* (8), 2792–2795. https://doi.org/10.1002/anie.201511432.

(59) Gorrini, C.; Harris, I. S.; Mak, T. W. Modulation of Oxidative Stress as an Anticancer Strategy. *Nat. Rev. Drug Discov.* **2013**, *12* (12), 931–947. https://doi.org/10.1038/nrd4002.

(60) Joshi, S.; Wang, T.; Araujo, T. L. S.; Sharma, S.; Brodsky, J. L.; Chiosis, G. Adapting to Stress — Chaperome Networks in Cancer. *Nat. Rev. Cancer* **2018**, *18* (9), 562–575. https://doi.org/10.1038/s41568-018-0020-9.

(61) Ahrné, E.; Molzahn, L.; Glatter, T.; Schmidt, A. Critical Assessment of Proteome-Wide Label-Free Absolute Abundance Estimation Strategies. *Proteomics* **2013**, *13* (17), 2567–2578. https://doi.org/10.1002/pmic.201300135.

(62) Henri, J.; Chagot, M.-E.; Bourguet, M.; Abel, Y.; Terral, G.; Maurizy, C.; Aigueperse, C.; Georgescauld, F.; Vandermoere, F.; Saint-Fort, R.; Behm-Ansmant, I.; Charpentier, B.; Pradet-Balade, B.; Verheggen, C.; Bertrand, E.; Meyer, P.; Cianférani, S.; Manival, X.; Quinternet, M. Deep Structural Analysis of RPAP3 and PIH1D1, Two Components of the HSP90 Co-Chaperone R2TP Complex. *Struct. Lond. Engl. 1993* **2018**, *26* (9), 1196-1209.e8. https://doi.org/10.1016/j.str.2018.06.002.

(63) Chauvin, B.; Nakazawa, K.; Beber, A.; Di Cicco, A.; Hajj, B.; Iv, F.; Mavrakis, M.; Koenderink, G. H.; Cabral, J. T.; Trichet, M.; Mangenot, S.; Bertin, A. Bottom-Up In Vitro Methods to Assay the Ultrastructural Organization, Membrane Reshaping, and Curvature Sensitivity Behavior of Septins. *J. Vis. Exp.* **2022**, No. 186, e63889. https://doi.org/10.3791/63889.

(64) Bissardon, C.; Reymond, S.; Salomé, M.; André, L.; Bayat, S.; Cloetens, P.; Bohic, S. Cell Culture on Silicon Nitride Membranes and Cryopreparation for Synchrotron X-Ray Fluorescence Nano-Analysis. *J. Vis. Exp.* **2019**, No. 154, 60461. https://doi.org/10.3791/60461.

(65) Villar, F.; Andre, L.; Baker, R.; Bohic, S.; da Silva, J. C.; Guilloud, C.; Hignette, O.; Meyer, J.; Pacureanu, A.; Perez, M.; Salome, M.; van der Linden, P.; Yang, Y.; Cloetens, P. Nanopositioning for the ESRF ID16A Nano-Imaging Beamline. *Synchrotron Radiat. News* **2018**, *31*

(5), 9–14. https://doi.org/10.1080/08940886.2018.1506234.

(66) Cesar da Silva, J.; Pacureanu, A.; Yang, Y.; Bohic, S.; Morawe, C.; Barrett, R.; Cloetens, P. Efficient Concentration of High-Energy x-Rays for Diffraction-Limited Imaging Resolution. *Optica* **2017**, *4* (5), 492. https://doi.org/10.1364/OPTICA.4.000492.

(67) Utica, G.; Carminati, M.; Fabbrica, E.; Ticchi, G.; Deda, G.; Borghi, G.; Zorzi, N.; Cloetens, P.; Cohen, C.; Salome, M.; Falkenberg, G.; Fiorini, C. High Rate SDD-Based Spectrometer for Energy-Dispersive X-Ray Fluorescence Detection. In *2021 IEEE Nuclear Science Symposium and Medical Imaging Conference (NSS/MIC)*; IEEE: Piscataway, NJ, USA, 2021; pp 1–3. https://doi.org/10.1109/NSS/MIC44867.2021.9875684.

For table of contents only